Title
SPECTRUM AND YIELD OF NEUTRONS FROM 31.5-Mev PROTON BOMBARDMENT OF SELECTED ISOTOPES OF COBALT AND NICKEL

Permalink
https://escholarship.org/uc/item/05g6x8vx

Author
Bostick, H.A.

Publication Date
1958-10-10

UCRL 8528

UNIVERSITY OF CALIFORNIA

Radiation Laboratory

SPECTRUM AND YIELD OF NEUTRONS FROM 31.5-Mev PROTON BOMBARDMENT OF SELECTED ISOTOPES OF COBALT AND NICKEL

DISCLAIMER

UCRL-8528
Physics and Mathematics

UNIVERSITY OF CALIFORNIA
Radiation Laboratory
Berkeley, California

Contract No. W-7405-eng-48

SPECTRUM AND YIELD OF NEUTRONS FROM 31.5-Mev PROTON BOMBARDMENT OF SELECTED ISOTOPES OF COBALT AND NICKEL

Hoyt A. Bostick

(Thesis)

October 10, 1958

Printed for the U.S. Atomic Energy Commission

Printed in USA. Price $2.50. Available from the
Office of Technical Services
U. S. Department of Commerce
Washington 25, D. C.

Contents

SPECTRUM AND YIELD OF NEUTRONS FROM 31.5-Mev PROTON BOMBARDMENT OF SELECTED ISOTOPES OF COBALT AND NICKEL

Hoyt A. Bostick

Radiation Laboratory
University of California
Berkeley, California

October 10, 1958

ABSTRACT

Protons from the University of California 31.5-Mev linear accelerator were used to bombard thin targets of Ni^{58}, Ni^{60}, and Co^{59}. Neutrons arising from the resulting reactions were detected with a 4-inch liquid hydrogen bubble chamber. Three spectrometer positions, 53°, 90°, and 127° in the laboratory system, were employed in measuring the angular dependence of neutron production from these targets. Energy spectra of neutrons with energies greater than 5 Mev were determined by reconstruction of recoil proton tracks in the liquid hydrogen.

Cross sections for neutron production were found in nickel to have an isotopic dependence; the yield of neutrons from Ni^{60} was significantly greater than that from Ni^{58}. The yield from Co^{59} exceeded that from Ni^{60} by a smaller amount. Angular distributions of the neutron spectra of all targets showed anisotropic characteristics.

The angular dependence observed for the neutron spectra from all targets has been interpreted as being composed of a combination of isotropic evaporation-type spectra and a distribution concentrated in the forward hemisphere which is characteristic of direct interaction processes. Occupation numbers for incompletely filled neutron shells in the nucleus may be related to the observed $Ni^{60} - Ni^{58}$ cross-section differences in the data.

I. INTRODUCTION

A. Nuclear Reaction Theory

Among the various ways to study the structure of matter developed since the advent of particle accelerators, one of the most widely pursued has been the investigation of nuclear reactions resulting from bombardment of complex nuclei by swiftly moving nucleons. Analyses of the reaction products arising from such bombardments are required in order to examine the collective behavior of a system of nucleons and to test predictions made by the various models for nuclear interactions. The descriptions of these reactions have been dependent upon the energy available for excitation of the projectile-target system, but there has been progress toward a satisfactory synthesis of the separate descriptions. The present state of these efforts has been summarized by Weisskopf.[1] A formulation which has proved to have wide applicability is that proposed by Bohr[2] and quantitatively developed by Weisskopf.[3] This process is understood as the independent formation and decay of a "compound nucleus" consisting of an amalgamation of the incoming particle and the target nucleus. A condition necessary for the validity of this viewpoint is that nucleon mean free paths be short compared with nuclear radii so that strong interactions will lead to rapid energy interchanges with all of the nuclear constituents. Decay of the compound nuclear system has been described quantitatively by use of a statistical viewpoint by Weisskopf,[3] with the result that the system is expected to be relatively long-lived because of the small probability that a single nucleon passess sufficient kinetic energy to escape. Decay should then be dependent on the energy of excitation but not explicitly on the mode of formation of the system. Some restrictions on this independence have been discussed by Wolfenstein.[4] One consequence of this decay mechanism is that the reaction products should be distributed symmetrically about a plane perpendicular to the incoming particle direction (when described in the center-of-momentum frame of reference); if many states of angular momentum are present, this symmetry should approach isotropy.[5]

In neutron emission, the absence of a Coulomb barrier to be penetrated simplifies the reaction-product energy spectrum expected on the basis of the statistical theory. An energy spectrum of emitted neutrons would appear to follow a Maxwellian distribution which might be characterized by a "nuclear temperature" parameter appropriate to the state of excitation of the residual nucleus.[6] This distribution of emitted neutrons would be expected to show a maximum at an energy that is small compared with the maximum available kinetic energy and decreases rapidly with increasing energy.

At energies high enough for the nucleon mean free path within nuclear matter to become comparable to the nuclear radius, the nucleus has been described by Serber as beginning to become transparent to the projectile.[7] The character of the reaction is then dependent upon the impact parameter; when the projectile passes through the nuclear edge only a single interaction can take place, whereas nearer the center of the nucleus there may be several collisions with much greater energy loss by the projectile. The latter process would be expected to give rise to the evaporation of particles from a highly excited nucleus with an energy spectrum similar to that expected at lower energies for the statistical decay of a compound nucleus. The energy spectra of neutrons emitted at 180° to targets bombarded by 171-Mev protons were measured by Skyrme and Williams[8] and found to be consistent with the evaporation theory. At small angles, reaction products with a high probability of escape without further interaction would be expected to appear along with the evaporation-particle spectrum.

For energies below the "transparent nucleus" region, anisotropic particle distributions have also been observed; for example, 32-Mev protons inelastically scattered from Sn, Ta, Au, and Pb were observed by Eisberg and Igo to have a strong forward peaking in the laboratory frame of reference.[9] Cross-section measurements were much higher than expected on the basis of particle evaporation theory, therefore a suggestion was made that the protons had undergone interactions near the nuclear surface where the nucleon density might be low enough to permit the reaction products to escape directly. Considerable attention has been given to calculation of angular distributions and cross sections for such "direct interaction" processes.[10]

B. Neutron Yields from Thick-Target Bombardment by 32-Mev Protons

In a systematic survey, of the total yield of neutrons arising from 32-Mev proton bombardment of thick targets, Tai et al. measured the yields of 59 elements and compounds and compared their results with calculations based on the statistical theory of nuclear reactions.[11] Their data indicated abrupt changes in the neutron yield at $Z = 20$ and $Z = 30$, and the yield from nickel was about one-third that of neighboring elements. These data in the region $Z = 26$ to $Z = 29$ are reproduced in Table I. To insure that these observations were not due to a resonance effect, the bombardments were also carried out by using 18-Mev protons. Tai et al. concluded that the observed effects were not a function of bombardment energy. It was shown by Millburn that a plot of the average neutron excess $\frac{N - Z}{A}$ against Z follows the same features as the yield data,[12] a result which is not predicted by the statistical theory. It was suggested by Tai et al. that these results might indicate a process whereby protons are captured into definite states of angular momentum accompanied by the emission of a neutron from a high-angular-momentum state, as suggested by Austern et al.[13]

C. Nature of This Investigation

The work described herein was initiated in an effort to study further the mechanisms responsible for the production of neutrons by 32-Mev proton bombardment in the region of the periodic table near $Z = 28$. It was desired to bombard thin isotopically pure targets with almost monoenergetic protons in order to measure the yield, energy spectrum, and angular dependence of emitted neutrons. Two elements were selected for study, cobalt and nickel. Naturally occuring cobalt consists solely of Co^{59}, which possesses 27 protons and 32 neutrons. Two isotopes of nickel having a combined isotopic abundance of 94.2%

Table I

Neutron yields for thick targets bombarded by protons;
10^{10} neutrons per microcoulomb of protons

Target	Bombarding energy (Mev)		
	0-32	0-18	18-32
Fe	6.00	1.00 ± .09	4.78
Co	8.20 ± .50	1.62 ± .18	-
Ni	3.06	0.32 ± .06	2.68
Cu	8.30	1.71 ± .12	6.45

Data from Tai, Millburn, Kaplan, and Moyer, Physical Review 109, 2086, (1958).

were chosen to permit examination in the light of the thick-target data of Tai et al. The major constituent, Ni^{58}, makes up 68.0% of natural nickel, while Ni^{60} contributes 26.2%. The proton number of nickel, Z = 28, is one of the so-called "magic numbers" associated with particular nuclear stability where, on the basis of the shell model, there is a closed f = 7/2 subshell.[14] A comparison of the data from Ni^{60} and Co^{59}, each of which has 32 neutrons, may indicate the effect on neutron emission of closure of a proton shell. Similarly, comparison of data from the two nickel isotopes might be expected to show the effects of outer-shell neutron occupation number when the proton configuration remains fixed. It is to be expected that these effects will become important as one examines neutron energies that are high compared with those expected on the basis of a particle-evaporation model.

D. Related Experimental Results

The absolute yields of low-energy neutrons (0.5 to 12 Mev) resulting from 190-Mev proton bombardment of Au, Ag, Ni, Al, and C have been determined by Gross,[15] using a nuclear emulsion technique. He reported observations at 45°, 90°, and 135° in the laboratory system; neutrons emitted from gold and silver targets showed distributions consistent with isotropic emission in the laboratory system, while an angular variation began to appear in spectra from nickel and became more pronounced in the case of aluminum and carbon. For energies above 3 Mev these variations were found to be inconsistent with an isotropic center-of-momentum distribution, and the observed spectra were attributed to the combination of (a) an isotropic evaporation process, and (b) an angle-dependent cascade process.

In the course of studying the relative energy-level density of several nuclei by the inelastic scattering of 18-Mev protons, Gugelot determined the proton energy spectra for nickel at 60° and 150° in the laboratory system.[16] He reported that the proton distribution showed some anisotropy, contrary to the result expected on the basis of evaporation theory. It was concluded that direct interactions of the protons with surface nucleons may have been responsible for the anisotropy, and that the observed spectra probably contained a significant portion of these contributions even for backward scattering angles.

In order to compare the energy distributions of protons from (n, p) reactions with results of inleastic scattering such as those reported by Gugelot, Ni^{58}, and Ni^{60}, as well as Al^{27}, Fe^{54}, Fe^{56}, and Cu^{63}, were bombarded with 14.1-Mev neutrons by Allan.[17] The observation angle was not varied for the nickel targets, therefore only proton energy distributions were examined. The spectra from Ni^{58} and Ni^{60} both appeared to contain more protons at the high- and low-energy ends than would be accounted for by a statistical theory. The spectra were consistent with the assumption that the low-energy component arose from (n,np) reactions, while direct interactions of the form (n, pγ) would account for the high-energy component. Using his experimental proton spectra to estimate the fraction of the (n, p) cross section that is due to decay of a compound nucleus, Allan computed the ratio of the level density of the residual nucleus produced by proton emission to that produced by neutron emission at the same excitation energy. He found that this ratio was 4.4 for Ni^{58} and 18.1 for Ni^{60}, and observed that these departures from unity may be due to the closed proton shell in Ni. At intermediate proton energies there was a resonably good fit of statistical curves to the energy spectra.

II. EXPERIMENTAL APPARATUS AND PROCEDURE

A. Introductory Remarks

Since the neutron does not possess electric charge, there exist no direct methods of detecting its passage and measuring its energy. There have been developed a variety of methods for detection based on observation of subsequent reactions induced by the interaction of neutrons with matter. The selection of a particular method is governed by the energy range of the neutron flux under consideration. In this case interest lies in the region of kinetic energies of several million volts. In principle, good energy resolution in this region can be obtained by analyzing recoil protons arising from neutron-proton collisions, and this method has been utilized in many studies concerned with neutron energy spectra. The proton recoils have been detected in two basically different ways, electronic and visual. Electronic counter telescopes indicate the passage of a charged particle by a coincidence requirement and determine the energy of the particle by measurements of range. Good resolution is obtained at the expense of efficiency because the proton radiator in which the n-p collisions take place must be made thin in order to reduce the proton energy loss by ionization; moreover, since the recoil-proton energy depends upon the direction of the proton with respect to that of the incoming neutron, the angular acceptance cone must be kept small. The visual techniques leave a record which can be subsequently analyzed to determine the incident-neutron energy. Recoil-proton tracks are photographed in a cloud chamber or rendered visible in developed nuclear emulsion plates. Since it is possible to deduce the incoming neutron energy from the proton energy and track orientation, there is no small-angle restriction, hence the geometric efficiency may be much increased. Owing to their gaseous interiors cloud chambers have a low density of target protons. Therefore they do not have a high efficiency and must be large to contain energetic recoil tracks. Chambers may be filled with hydrogen gas in order to minimize the occurrence of inelastic events. Nuclear emulsion plates present a higher concentration of target protons to a neutron flux than does a cloud chamber and have been rather widely utilized for neutron spectroscopy. It is necessary, however, to distinguish between elastic and inelastic events within the emulsion, owing to the presence of many complex nuclei.

Development of liquid-hydrogen-filled bubble chambers[18] has made available moderately dense concentrations of protons which are free from neighboring complex nuclei. The bubble-chamber technique allows recoil tracks to be made visible and photographed in the liquid hydrogen itself, thus combining some of the desirable characteristics of both the cloud chamber and the nuclear emulsion. A small number of tracks may be recorded on each of a large number of photographs in order that scanning efficiencies may be made high. The sensitivity of a bubble chamber to the ionizing power of a particle may be controlled in order that tracks due to electrons may be reduced greatly or entirely eliminated. The 4-inch-diameter liquid-hydrogen bubble chamber was found to have a 4% efficiency for detecting 10-Mev neutrons (Appendix B), hence when accompanied by a track-reconstruction scheme which is rapid and accurate it would seem to offer a very useful neutron spectrometer. Accordingly, the 4-inch chamber was chosen for use in this experiment.

B. Targets

Targets consisting of a high concentration of single isotopes of cobalt and nickel were desired for bombardment in this experiment. Since there is but one stable isotope of cobalt, that with mass 59, it was necessary only to obtain a sample with high purity and suitable thickness from a commerical source.* Stable nickel isotopes having mass numbers 58 and 60 were obtained from the Stable Isotopes Division of the Oak Ridge National Laboratory. These samples were supplied in the form of nickel oxide (NiO), therefore it was desired to reduce the oxides

---

*A. D. Macay, Inc., 198 Broadway, New York, N. Y.

to metallic form in order that targets relatively free from oxygen contamination could be fabricated. The reductions were carried out by heating in a hydrogen atmosphere, and the metal powder was then sintered to form 1-inch-diameter disks with thicknesses appropriate for a 1-Mev proton energy loss at 32 Mev.* This target thickness was chosen as that leading to optimum neutron production with the beam currents available under the operating conditions encountered at the linear accelerator. Table II shows the isotopic purity, areal density, and proton energy losses for each target. Values for proton energy losses were computed by an interpolation method using the range-energy tables constructed by Aron et al.[19]

C. Beam Collimation and Shielding

Bombardments were carried out by using the 31.5-Mev proton beam from the University of California proton linear accelerator.[20] Near the exit end of the machine a steering magnet deflected the beam through an angle of 20° whereupon it passed into a strong-focusing quadrupole set that was adjusted to give a minimum beam diameter at the target position. Carbon collimators, 3/4 inch in diameter, were placed behind the steering magnet and the quadrupole set in order to reduce the spurious production of neutrons by protons scattered in these magnets. There was a 1/2-inch carbon collimator immediately ahead of the 2-foot-thick concrete wall separating the inner and outer bombardment areas, and a second 1/2-inch carbon collimator about 30 inches in front of the target position. The locations of these collimators and the magnets are shown in Fig. 1.

A target chamber was designed that could accommodate nine separate targets on a "ladder" adjustable through a pair of Wilson seals. The body of the chamber was rolled from 1/8-inch aluminum sheet with a 2-inch-diameter beam entrance pipe and a 3-inch-diameter exit pipe.

---

*Reduction and sintering operations were carried out at the U.C. Radiation Laboratory, Livermore, California, by Mr. Eldon Westlund of the metallurgical group.

Table II

Isotopic purity of target materials

Target material	Isotopic distribution (%)						ρ (gm/cm^2)	ΔE (22.5°) (Mev)
	Co^{59}	Ni^{58}	Ni^{60}	Ni^{61}	Ni^{62}	Ni^{64}		
Ni^{58}	...	99.6	0.3	...	0.1	...	0.1109	1.46
Ni^{60}	...	0.8	99.1	0.06	0.02	0.006	0.0893	1.13
Co^{59}	99.9	...	...	...	...	...	0.0684	0.859

Isotopic purity of nickel oxide samples: data furnished by Stable Isotopes Division, Oak Ridge National Laboratory.

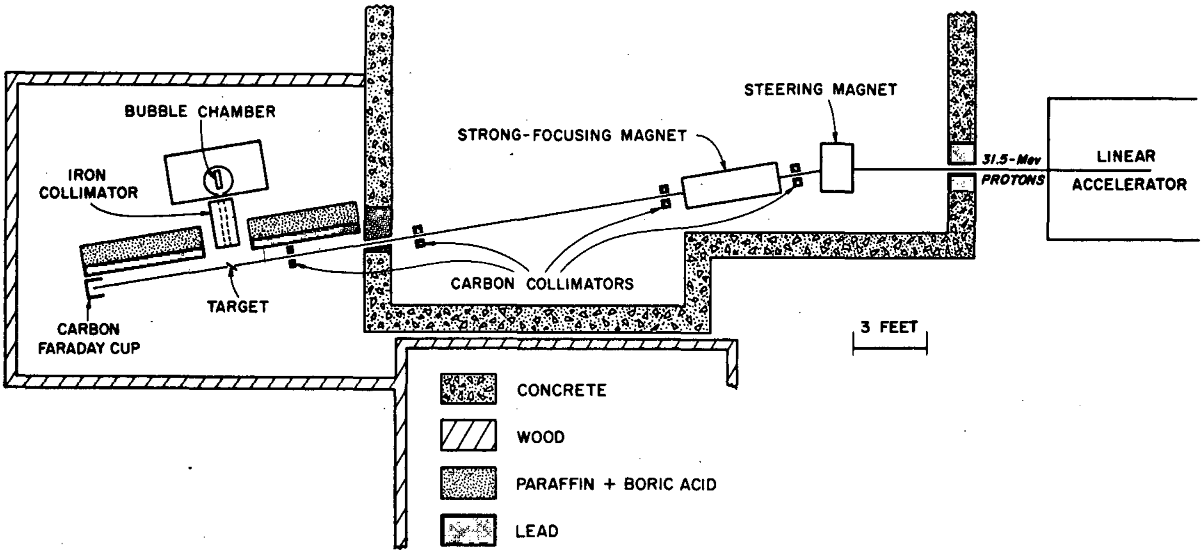

Fig. 1. Schematic diagram of linear accelerator, magnets, collimators, shielding, and bubble chamber location.

Both entrance and exit pipes were lined with a 1/4-inch layer of polyethylene in an effort to reduce the production of neutrons by scattered protons. Lucite-covered windows were provided around the center of the holder to allow accurate positioning of a neutron collimator between the target chamber and the entrance window of the bubble chamber. (The target chamber can be seen in Fig. 5, showing the bubble chamber in position.)

Beyond the target chamber the diameter of the beam vacuum pipe was increased to 6 inches to partially compensate for spreading of the proton beam introduced by multiple scattering in the target. Six feet behind the target holder, the proton beam was stopped in a carbon Faraday cup of 6-inch diameter. A 4-inch layer of lead bricks was placed alongside the large-diameter beam pipe to attenuate gamma rays that might produce a background of electrons in the bubble chamber. Outside the lead layer an additional 16-inch wall of wooden boxes filled with a mixture of paraffin and boric acid reduced the chance that neutrons produced in the polyethylene liner could get into the bubble chamber.

D. Liquid Hydrogen Bubble Chamber

The 4-inch liquid hydrogen bubble chamber selected for use during this experiment has been described in some detail elsewhere.[18, 21] An important aspect of chamber operation for the purposes of neutron spectroscopy is the variation with temperature of chamber sensitivity to the ionizing power of a charged particle. This property of the chamber allowed a mode of operation whereby proton tracks were plainly visible whereas the passage of an electron left virtually no visible record. Variation in chamber temperature had to be kept within 1/10°C in order to keep within the limits of good proton visibility without electron sensitivity. This was a difficult requirement, but it was met with moderate success after the heat-regulation system was modified to the type employed in the 10-inch liquid hydrogen bubble chamber at this laboratory. Although the chamber had been equipped with magnetic-field-producing coils, they were removed during the course of this work in order to eliminate a possible source of in-scattered neutrons. The orientation of the bubble chamber with respect to the neutron beam defined by a collimator is shown in Fig. 2. A 1/8-inch plexiglas window was installed in the outer vacuum vessel to aid in aligning the neutron collimator. The bubble chamber entrance window was a stainless steel disc having a 7/8-inch diameter and 0.001-inch thickness. The camera and stereo axes, both perpendicular to the incoming neutron direction, are also indicated in Fig. 2.

Sensitivity of the chamber to the presence of charged particles was achieved by a rapid reduction in applied gas pressure immediately prior to the expected traversal of particles. After sufficient time had elapsed to allow the growth of bubbles along a track, a xenon-filled flash tube was fired to photograph the event. A schematic representation of the chamber-pressure display is shown in Fig. 3. This display was presented by a dual-trace oscilloscope in order that timing signals for the beam passage and light flash could be superimposed on the pressure curve. The expansion, suitably delayed from the preceding linac trigger pulse, was timed so that the beam pulse occurred at the minimum of the pressure stroke, then the light was flashed 6 milliseconds after the beam pulse. Immediately following the light pulse a rapid recompression stroke returned the chamber to its initial pressure before the onset of general boiling with its consequent loss of heat. Timing of all the aforementioned functions was provided by a number of delay chassis contained in the bubble chamber control rack. This rack, shown in Fig. 4, was located in the linac counting area for accessibility at all times during the course of a run. All data were recorded by a motor-driven remotely controlled 35 mm Recordak stereo camera mounted 18 inches in front of the chamber. "Dark-field" illumination was provided by a small but intense light source a short distance behind the glass back of the chamber and putting a large lens immediately behind the chamber, which caused the whole of the chamber to be illuminated but focussed the light on a small area between the two lenses of the stereo camera. Hence light entering the camera lenses was scattered by bubbles through very small angles. The bubbles showed up as very

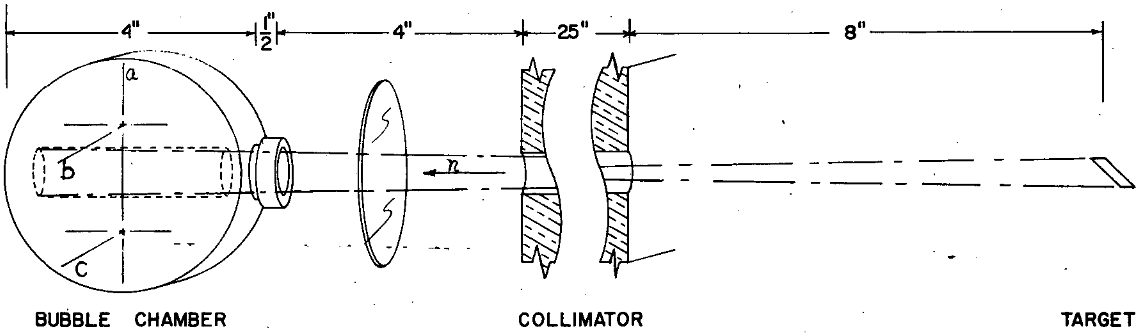

MU-16103

Fig. 2. Orientation of bubble chamber and neutron collimator. Cylinder inside chamber denotes the acceptable track region. The stereo axis is indicated by (a), with (b) and (c) the upper and lower lens axes.

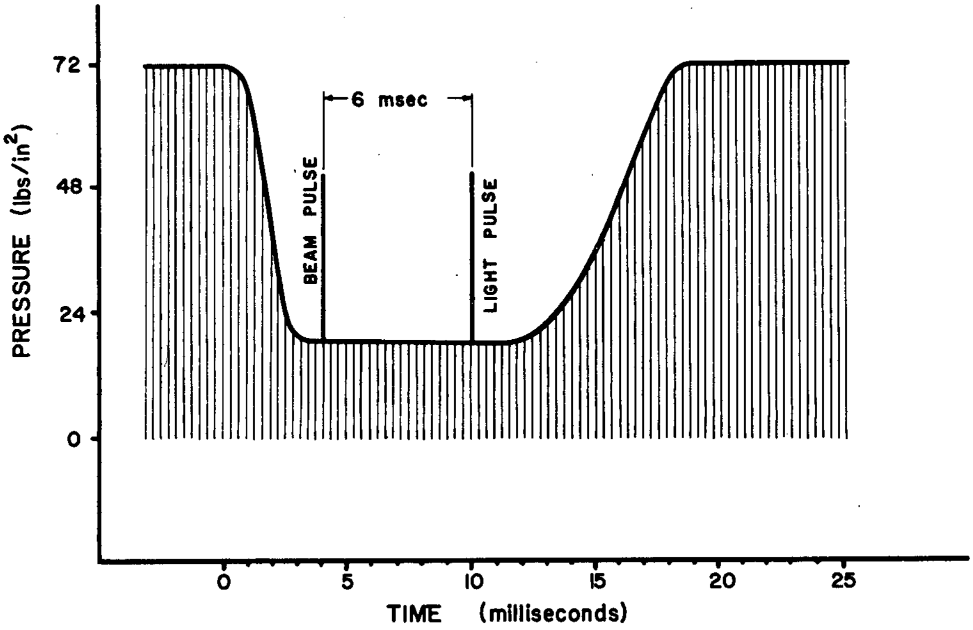

MU-16104

Fig. 3. Schematic oscilloscope display of bubble chamber pressure, showing proton beam and photographic light-timing pulses.

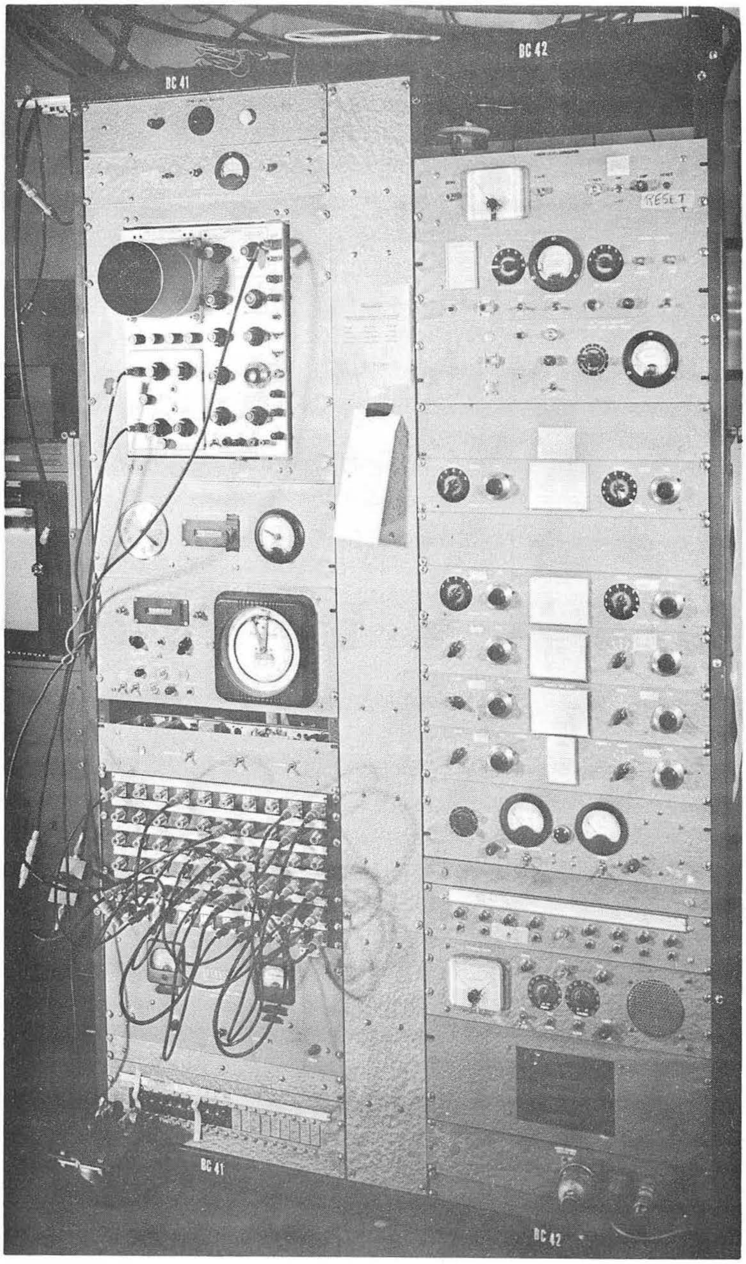

ZN-2048

Fig. 4. Liquid hydrogen bubble chamber control **rack.**

intense light sources in a dark field, therefore the lens diaphragms could be kept small. With the film used, Kodak Panatomic X, lens diaphragm settings of f/22 were quite adequate and good depth of field in the photographs was obtained. Rapid determination of chamber sensitivity and track density was made possible through use of a Polaroid-Land camera located behind a remotely controlled mirror which could be placed so as to cut off the stereo camera's view and place an image of the chamber before the Land camera. This allowed a single-lens photograph of the chamber to be obtained in slightly more than a minute so that any changes required in operating conditions or beam intensity could be made without the necessity of waiting to process the ordinary film.

For purposes of this experiment, the bubble chamber table was mounted on a low platform which pivoted around the target position, allowing rapid and accurate variation of the neutron-acceptance angle. A table to support the neutron-beam collimator was mounted in front of the bubble chamber. Figure 5 shows the bubble chamber, collimator, and pivoting platform in relation to the target holder.

E. The Neutron Collimator

In an effort to restrict neutron entrance into the chamber to those neutrons which had passed through the thin steel window, an iron collimator 6 × 4 × 25 inches was aligned between the target holder and the wall of the chamber's vacuum vessel. Provision for closing the hole for background determination was made by fabricating the collimator from four 1-1/2×4×28-inch bars. The upper two were cut in half for greater ease of handling. A partially disassembled collimator is shown in Fig. 6. A 1-inch hole through the center of the inner two iron bars allowed insertion of smaller-bore brass collimators or a brass "plug." Aside from some tests described in Section IV-A, all data runs were made with a hole diameter of 5/8 inch, which just exposed the entrance window of the chamber with the collimator position used. The collimator rested on a short U beam supported by three small screw jacks. Four bolts located on the sides of the U beam provided horizontal adjustment,

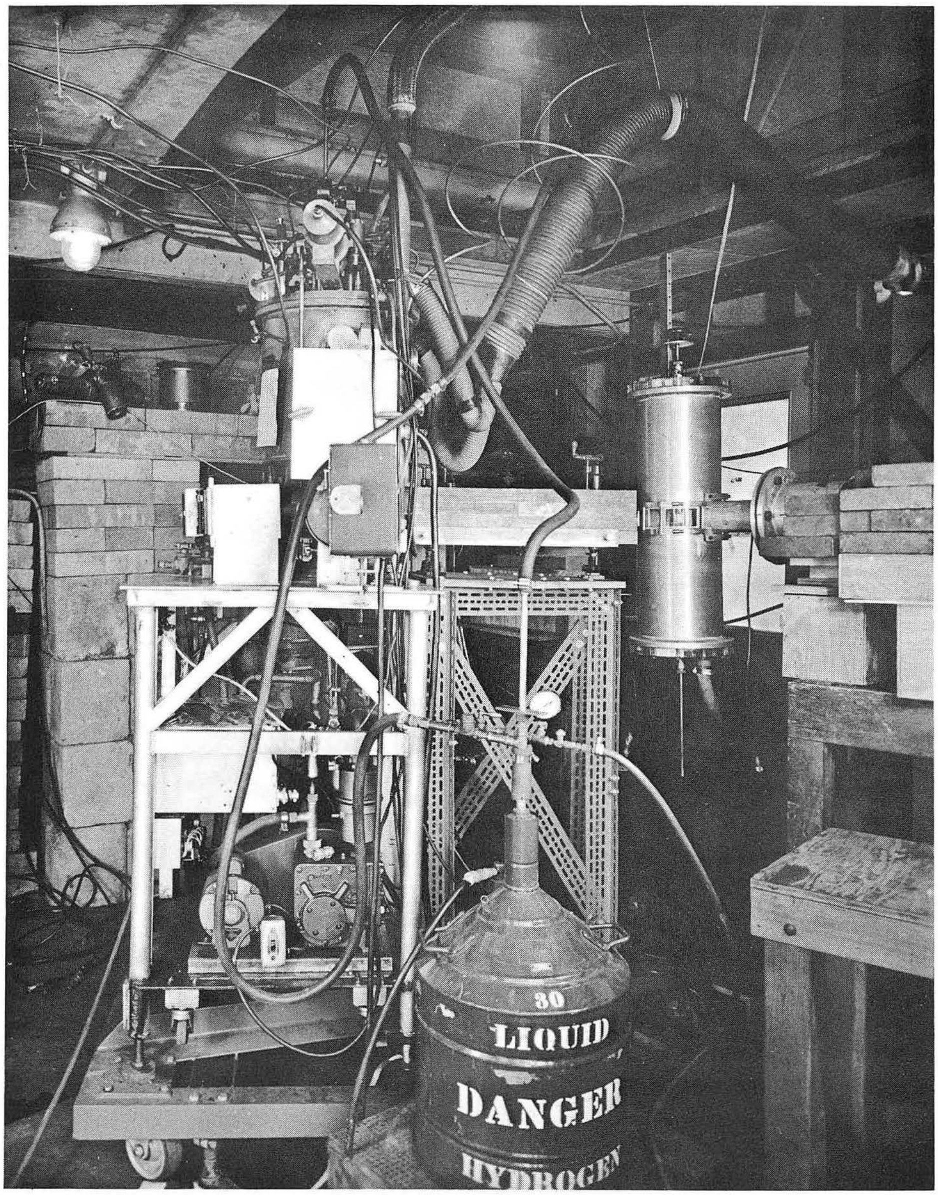

ZN-2049

Fig. 5. Liquid hydrogen bubble chamber, neutron collimator, and target chamber in bombardment position. Shielding around beam exit pipe has been removed to permit photograph to show target chamber.

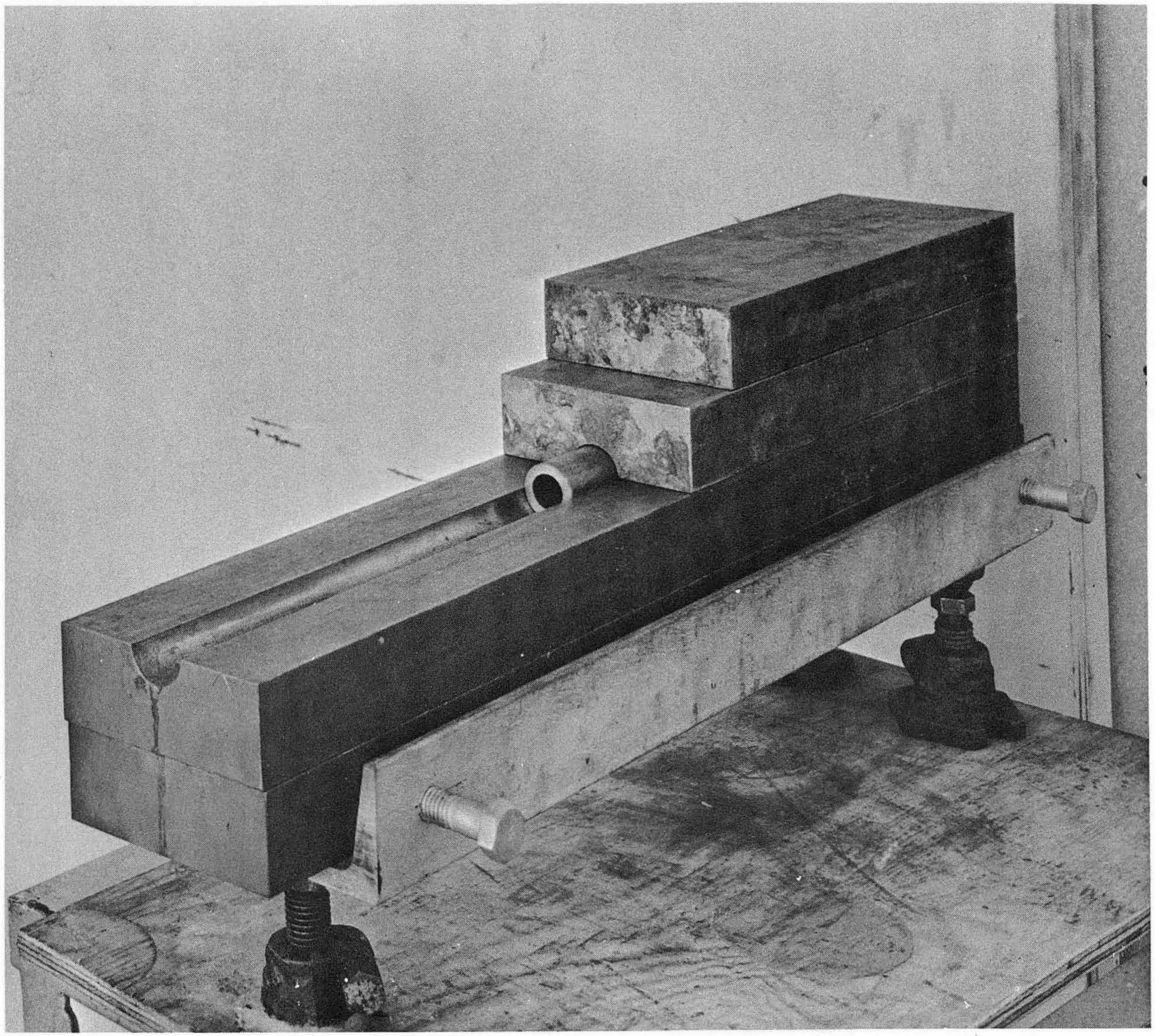

ZN-2050

Fig. 6. The neutron collimator partially disassembled, with the supporting U frame and adjustable jacks.

so that quick and precise alignment could be effected whenever necessary. Some additional plates of iron were inserted underneath the U beam for additional protection from scattered neutrons coming from below. Smaller plates having a total thickness of about 1 inch were added to the top to reduce the neutron flux striking the upper parts of the chamber structure, thus further reducing stray scattering into the chamber.

F. Bombardment Technique

Both the liquid hydrogen bubble chamber and the linear accelerator were pulsed devices; however, the linac pulsed 75 times during the 5-second period of the bubble chamber. There were two compelling reasons for accelerating a proton beam only when the chamber could be made sensitive; first, to allow an accurate determination of the amount of beam passing through the target while the chamber is sensitive, and second, to reduce by a factor of 75 the amount of stray neutron radiation around the accelerator area. This operating mode was easily achieved, for the need for a similar mode of operation had been successfully met for cloud chamber experiments done in the past. The technique was that of dephasing the 15-cps pulses of the Van de Graaff generator with respect to those of the linac at all times when a proton beam was undesirable, then bringing them into phase for a single pulse when the bubble chamber was sensitive. In this fashion only protons that bombarded the target when the chamber was sensitive were collected by the Faraday cup. Charge on the Faraday cup was integrated across a precision condenser having a known calibration, and the voltage across this condenser was measured by a conventional UCRL feedback electrometer in conjunction with a Leeds and Northrup Speedomax recorder. The record of integrated beam consisted of a series of step displacements, each of which could be identified with a particular picture number, if necessary. In most cases, however, only the total collected charge was of interest.

Targets were oriented at an angle of +22.5 degrees to the proton beam during 53° and 90° bombardments, and at -22.5 degrees for the 127° bombardment. The forward angle was selected as being the minimum obtainable because of the size of the bubble chamber table. The 127° position was selected to give data points symmetrically located about 90°. Each data run consisted of exposing a 100-foot roll of film (400 stereo picture pairs) with the collimator hole open. Background runs consisted of a like amount of film exposed with the collimator closed. Target-out runs were found to be quite unnecessary, as the film was virtually blank in every case.

Since a correction for beam loss due to scattering by the targets was necessary, the fraction of beam loss was experimentally determined. This was accomplished by providing a monitor of beam intensity independent from the Faraday cup, and measuring ratios of beam collection with targets in and targets out for a constant beam intensity. The beam-intensity monitor chosen was a 2-mil gold wire scatterer which elastically deflected protons through a thin window in the beam pipe and into a well-shielded scintillation counter. The scintillation counter signal was fed into a ten-channel pulse-height analyzer set with the elastically scattered proton pulses well separated from lower-energy events. The gold wire was mounted on a frame which could be moved in and out of the beam by means of a remotely controlled solenoid. This allowed the measurement of proton background in the counter for any beam level. A further check on the accuracy of the method was made by comparing the scintillation counter's rate with the Faraday cup for several different beam intensities with targets removed. Very good agreement was found between these two monitors. Ratios of target-in to target-out beam collections were found by running for a given number of counts in the elastic-peak channel and measuring the charge collected by the Faraday cup with the condenser and electrometer used in the remainder of the experiment.

G. Resolution and Background Check

In order to show that the bubble chamber, together with its surroundings and the data-analysis scheme, was capable of determining the energy spectrum of a neutron flux, a resolution determination was desired which would employ almost monoenergetic neutrons arising from the reaction $d + t \rightarrow He^4 + n$. These neutrons, which are produced by deuterons of low energy, have an energy of 14.1 Mev at 90° in the laboratory system.[22] Targets of tritium absorbed in titanium were available at the Livermore laboratory; therefore it was decided to attempt the bombardment of tritium with 4-Mev deuterons, accelerated by the Van de Graaff generator, which subsequently "coast" through the unused linear accelerator tank. Trials with singly ionized hydrogen molecules showed that an intense beam of mass - 2 particles could be obtained at the target position used during the experiment. In order to avoid producing large numbers of stray neutrons arising both from deuteron disintegrations and the d-t reaction, it was desired to pulse the Van de Graaff generator only when the bubble chamber was made sensitive. This presented a slightly different problem from that of preventing proton acceleration. Since the Van de Graaff generator was an electrostatic machine, it was necessary to pulse its ion source with a signal derived from the bubble chamber control system. Under ordinary operating conditions the ion-source pulse was derived from the flash of a 15-cps light source at the grounded end of the accelerator and directed toward a phototube at the high-voltage end. Single-pulse operation was obtained by replacing the pulsed power source for the light with a capacitative discharge initiated by the bubble chamber timing chassis.

The titanium in the target available had an areal density of 6.9 mg/cm^2, which was sufficient to stop a 2-Mev deuteron beam. A gold foil that would degrade 4-Mev deuterons to 2 Mev was interposed in front of the titanium disk. A dummy target with similar characteristics but without tritium was provided for bombardment in order to demonstrate that the neutrons observed originated from the d-t reaction.

Runs were made with several variations in the neutron collimation used: with a 7/8-inch-diameter hole, a 5/8-inch-diameter hole, and no collimator, as well as with the collimator hole closed with a brass plug. A relative measure of the deuteron beam was obtained by connecting the electrometer to the target holder frame that was insulated from the walls of the vacuum system. An example of the recoil tracks from these 14.1-Mev neutrons is shown in Fig. 7.

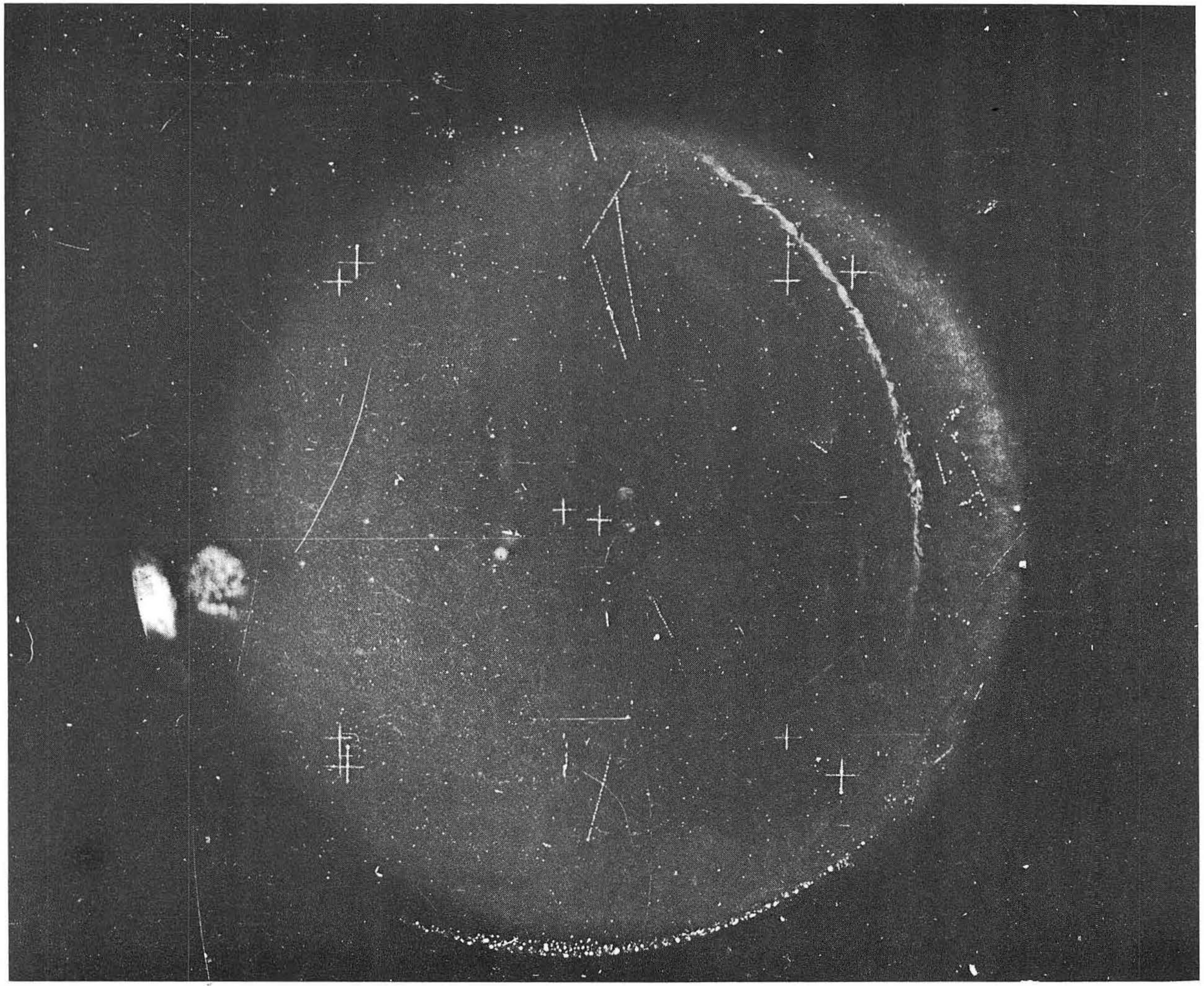

ZN-2051

Fig. 7. Proton recoils from neutrons arising from the T(d, n) He^4 reaction, photographed in the 4-inch liquid hydrogen bubble chamber.

III. RECOIL-TRACK ANALYSIS AND DATA REDUCTION

A. Introductory Remarks

Reconstruction of a spectrum of neutron energies from an analysis of recoil-proton tracks is based on well-known properties of neutron-proton collisions. The basis for such reconstruction is that the energy of a recoiling proton and the angle it makes with the incoming neutron's incident path determine the energy before collision of that neutron. Hence measurements of the ranges of recoil protons (when the appropriate range-energy relation is known) and their orientations are sufficient to allow a construction of the incoming neutron energy spectrum. It is shown in Appendix A that the length and orientation of a track are determined when the end points are located in each member of a stereo pair of photographs. A useful analysis procedure must include a rapid and accurate method of recoil-track measurement and an equally efficient means of making simple but tedious calculations. The latter requirement can be easily met by utilizing a high-speed electronic digital computer, which is easily programmed to repeat hundreds of similar calculations in a very short time. The IBM 650 type data-processing machine available at this laboratory worked from a punched-card input, and thus suggested the nature of a satisfactory solution to the first requirement above. If each member of a stereo pair of photographs were to be projected in turn on a screen, it would be possible to read the Cartesian coordinates of each end of a track and record these data on a card suitable for use in the data-processing machine.

B. Equipment

A commercial coordinate-reading device, named the "Oscar,"(*) could furnish a digital read-out of x and y coordinates of points on a projected image. When combined with a projection system suitable for use with stereo photographs and an IBM card punch, the Oscar would be able to provide the track end-point data necessary for the analysis program.

---

*Manufactured by the Benson-Lehner Corporation, Los Angeles, California.

An ordinary home-type 35mm stereo projector was extensively modified to adapt it for use with the Oscar. Changes and additions included: (a) installation of a glass-plate-type film carrier with solenoid-operated film release, (b) motorized film takeup and rewind mechanism with 100-ft-roll capacity, (c) remotely controlled lens holder providing horizontal and vertical lens adjustment, (d) remote focus control for the lens mount, (e) a heavy-duty cooling fan allowing continuous operation, and (f) a solenoid-operated shutter system which provided for separate or simultaneous observation of the two views constituting a picture pair. The shutter system was operated by a semiautomatic control chassis which, upon the completion of two data entries (corresponding to the coordinates of each end of a track) for one view, changed to the second view in the same frame. Another chassis acted as an automatic counter or accumulator which assigned an identification number to each track that was measured. This chassis supplied an appropriate signal to the card punch at a preselected column on a data card and thus relieved the reader of the necessity of counting tracks or recording track numbers. Figures 8 and 9 show the track-recording equipment, including the Oscar, the stereo projector, its housing and 45° mirror, the IBM card punch, and the rack for track-identification and control chassis.

C. Method of Track Measurement

The basis for the track-analysis scheme is described in Appendix A, where it is shown that the true length of a track can be determined directly from relative coordinate measurements of the track end points in stereo views. However, it was necessary to know the location of a track in space in order to insure that certain criteria were met before the track could be considered acceptable. (These criteria are considered in detail in Part E of this section.)

In order to locate the tracks in the chamber, two kinds of data cards were employed in the film-reading process. A "master card" identified each frame and a "track card" was made for each track observed in the frame. The master card contained the observed coordinates of a

ZN-2052

Fig. 8. Track-analysis equipment; left to right, IBM card punch, "Oscar," and track accumulator.

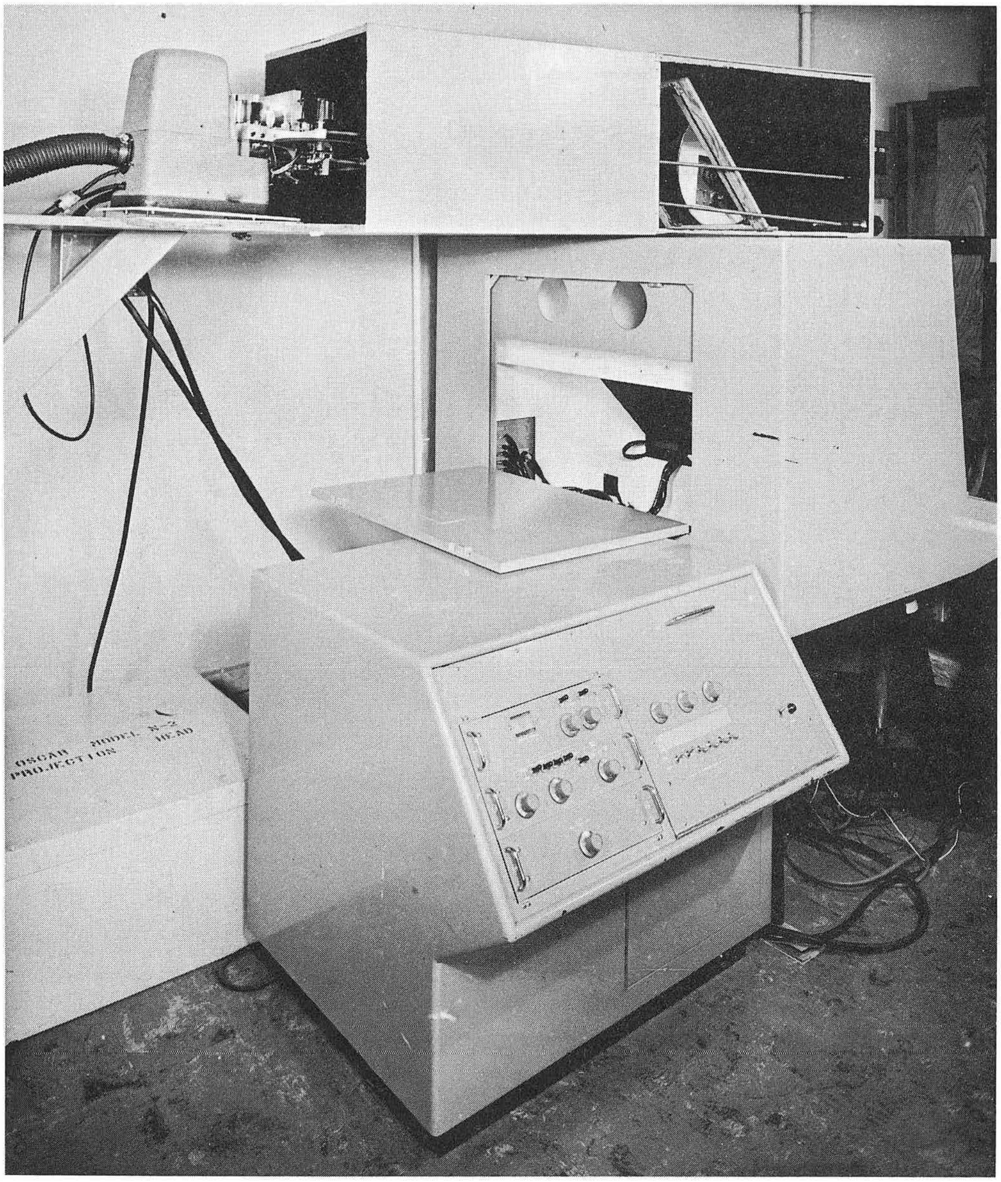

ZN-2053

Fig. 9. Rear view of the Oscar, showing the projection system added for stereo photographs.

fiducial mark located on the bubble chamber glass, and thus permitted subsequent track data to be referred to a coordinate system fixed in the bubble chamber.

Every card, whether track or master, received an identification number consisting of (a) the data run number, (b) the frame number, and (c) the track number. A master card was assigned a track number of zero in order to distinguish it from a track card.

Since only the track number in the identification number differed for individual cards belonging to a single frame, it was necessary to punch the run and frame numbers manually only once and allow the duplication punch mode of the IBM card punch to reproduce them on all succeeding cards belonging to the same frame. The run number, constant throughout an entire roll of film, was stored in the Oscar and could be read in the first (i.e., the master) card by merely pressing a button. The frame number was entered on that card by means of the keyboard on the IBM punch unit; this number consisted of the final three digits displayed on a counter photographed during each bubble chamber expansion.

The track number, entered automatically by the track accumulator, was advanced by one unit for each succeeding card until reset by a special "end-of-frame" button when a sequence was completed. Following the identification numbers on a card came the data entries.

Two entries, corresponding to the coordinates of the fiducial mark in each view, were required for each master card. The control chassis changed views after each data entry here, rather than after each second entry, as for track cards for which two points in each view were required.

Because the usable region of the chamber was smaller than the chamber dimensions, it was desirable to give the observers an indication of the acceptable region of the chamber. (The purpose was to effect a saving of reading time by preventing tracks far removed from the acceptable region from being recorded.) This was accomplished by mounting over the viewing screen an adjustable overlay of clear plastic having two parallel lines indicating the extent of the arbitrarily selected region. This device was deliberately made slightly oversized in order that all final rejections would be made during the computing program. With this system, a skilled observer could read an hourly average of ten frames each of which might contain from six to ten recoil tracks.

Occasionally the magnification of the entire optical system was redetermined by measuring the horizontal and vertical separation of fiducial marks on the front and rear glasses of the chamber. These measurements were used to compute the "g factors" defined in Appendix A. It was found that they held quite constant through the entire data-accumulation period, and all the computations were made by using a single set for all runs.

D. Kinematics of Neutron-Proton Collisions

It is an elementary result of particle kinematics that the non-relativistic collision between particles of equal mass, one of which is initially at rest, results in the particles' moving off at right angles to each other. The kinetic energy of a recoiling particle is related to the kinetic energy of the incident particle by a factor equal to the square of the cosine of the angle between the directions of incidence and recoil. Specifically, in the case of interest for this work with neutrons incident upon hydrogen, one has

$$E_p = E_n \cos^2\theta_L, \tag{1}$$

where E_p is the recoil energy of the proton, E_n is the initial neutron energy, θ_L is the laboratory-system angle between the momentum vectors (cf Fig. 10).

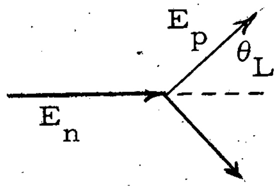

Fig. 10. Recoil of proton struck by a neutron-lab system.

In the center-of-momentum frame of reference, the velocity vectors of proton and neutron are always equal and opposite; after collision the proton appears to recede at an angle equal to twice that observed in the laboratory frame. $\theta_c = 2\,\theta_L$ cf Fig. 11. (2)

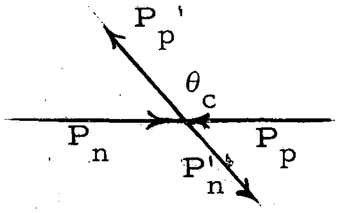

Fig. 11. Recoil of a proton struck by a neutron--c.m. system.

In order to discuss the proton angular distributions to be expected, it is necessary to examine the transformation of the n-p scattering cross section from the center-of-momentum system to the laboratory system. Since all particles scattered into a given solid angle in the first system will be scattered into an equivalently transformed solid angle in the second system, the cross-section transformation can be expressed as

$$\left(\frac{d\sigma}{d\Omega}\right)_L d\Omega_L = \left(\frac{d\sigma}{d\Omega}\right)_C d\Omega_C, \tag{3}$$

where the subscript L refers to the laboratory frame and C to the center-of-momentum frame. The quantity conveniently measurable is $\left(\frac{d\sigma}{d\theta}\right)_L$, which can be written from Eq. (3) as

$$\left(\frac{d\sigma}{d\theta}\right)_L = \left(\frac{d\sigma}{d\Omega}\right)_C \frac{d\Omega_C}{d\theta_L} = \left(\frac{d\sigma}{d\,\Omega}\right)_C (4\,\pi \sin\, 2\theta_L). \tag{4}$$

For neutron energies less than 10 Mev, the n-p scattering cross section can be taken to be isotropic in the center-of-momentum frame.[22] Hence the laboratory-system angular distribution of a specific neutron energy range is proportional to sin $2\theta_L$. This fact allows a convenient check on the observed results, which was utilized as described in Section IV-B.

Energies of the observed recoil protons needed to be determined from a suitable range-energy relation. The tables of Aron et al.[19] were used to compute the range of protons in hydrogen, and the data of Stevenson[23] to determine the density of superheated liquid hydrogen under the conditions encountered in the experiment. These data were found to fit the relation $R = aE^{1.84}$, where R is the range in centimeters, E is the energy of the proton, and a is a constant which depends upon the density of liquid hydrogen. For a density of 0.059 g/cm^3, appropriate for this work, the numerical value of a was determined to be 0.0126.

In order to compute the variation of neutron-detection efficiency with neutron energy it was necessary to know the energy dependence of the total neutron-proton scattering cross section. A table of cross sections as a function of energy for neutron-energy increments of 0.2 Mev between 3 and 30 Mev was prepared from the compilation by Hughes and Harvey.[24]

E. Data Processing

The computational procedure used to determine the energies of recoil protons and the associated neutrons is described in Appendix A. It is in order here to discuss the acceptance criteria by which tracks were judged. As indicated earlier, only data on neutrons that had passed through the thin window in the chamber wall before colliding with a proton were desired. This meant that only recoil-proton tracks observed inside a cylindrical region having a diameter of 7/8 inch were permitted. The method of determining which tracks met this requirement is indicated in Appendix A. Calculation was discontinued on tracks that began outside the allowed region, and the machine passed on to the next data card. All remaining track data were carried through the entire calculation; later rejections were made by including a "minus" punch and a code numeral indicating the reason for rejection on the track answer card. Rejected tracks lying inside the allowed region were included in the answer cards in order to allow further study of these data. A rejection was recorded for a track whose terminus lay beyond a plane defining the longitudinal extent of the allowed cylindrical region. Similarly, the point of collision was required to be inside a plane defining the beginning of the cylindrical region. It should be noted that the terminus of a track was permitted to lie outside the circular wall of the allowed cylinder. It can be shown that no track having an energy attainable in this experiment could escape through the front or rear glass plates of the chamber. A rejection of tracks ending in the glass plates was included in the program, however, as a safeguard against inclusion of erroneous measurements in the data print-out. (This proved quite unnecessary; that rejection code never appeared among the answer cards.) The recoil length, polar angle, and azimuthal angle were included as a part of the answer punch-out. The energy of each proton was determined from the range-energy relation, which was stored in the 650 in tabular form. Entries in the table were spaced at 0.1-Mev intervals for energies between 3 and 12 Mev and at 0.2-Mev intervals between 12 and 32 Mev. A tabular form was adopted in order to avoid the complexities of repeated calculations from the exponential range-energy relation. Only recoil protons within the angular range $0^\circ \leqslant \theta_L \leqslant 30^\circ$ were considered acceptable tracks. This choice was made on the basis of measured line shapes resulting from d-t neutron measurements, and was related to the increased energy resolution obtainable as the maximum value of θ_L is reduced. It was also found that significantly fewer spurious high-energy neutrons were included in spectra having a 30° limit than in those with a limit of 45°. All answer cards with a value of θ_L greater than 30° received a "minus" punch and a code number for angular rejection. The energy of the incoming neutron was computed from Eq. (1) and punched into the track answer cards. In addition to the answer-card punch, each acceptable track was recorded in a neutron-energy spectrum which was stored in the memory until the completion of a data run. Similarly, recoil-proton angular-distribution spectra were constructed for 5-Mev increments in neutron energy. In order to allow more complete analysis of results it was desired to know where along the chamber axis the n-p collision took place. This information was also punched into each track answer card so that subsequent data-processing programs might make rejections based on track length and collision location. At the end of a series of track-measurement cards constituting a run, a summary card was inserted into the machine. This card initiated a punch-out of the stored distributions.

F. Neutron-Production Cross Sections

Since the neutron-proton scattering cross section is dependent upon energy, a neutron detector based on analysis of n-p collisions requires that account be taken of this energy dependence. As the kinetic energy of the particles is increased, the scattering begins to show some anisotropy in the center-of-momentum system. Both these effects were accounted for in a way described in Appendix B, in which is discussed the construction of a table of factors that transform observed neutron numbers into magnitudes of neutron flux incident upon the detector. A neutron-production cross section, defined in the usual way, was written in terms of the neutron flux observed between the energies E and E + dE:

$$\frac{d^2\sigma(E_n)}{d\Omega dE_n} = \frac{\left(f_{(\epsilon_n)}\,\Delta E_n\right)}{N_p N_t \Delta\Omega\Delta E}, \qquad (6)$$

where

$f_{(\epsilon_n)} dE_n$ = the flux of neutrons within an energy range ΔE_n within the solid angle $\Delta\Omega$,

N_p = the number of incoming protons,

N_t = the number of target nuclei per unit area,

$\Delta\Omega$ = the solid angle subtended by the detector,

ΔE = the energy range chosen for the determination.

The number of incident protons, N_p, was given by the total charge collected by the Faraday cup (corrected for losses), divided by the unit of elementary charge,

$$N_p = q/e \ ,$$

where q was expressed as $q = R_t\, nCV$,

with R_t = measured charge-collection correction,

n = electrometer deflections or "dumps,"

C = capacity of condenser,

V = voltage on condenser for a full-scale electrometer deflection.

Values of R_t for each target are given in Table III.

Table III

Beam charge-collection correction and target characteristics

Target	Charge-collection ratio	Areal density (g/cm^2)	Target nuclei unit area
Cobalt-59	1.22 ± .08	0.0684 g/^{2}	$0.756 \times 10^{21}/\text{cm}^2$
Nickel-58	1.40 ± .05	0.1109 g/^{2}	$1.246 \times 10^{21}/\text{cm}^2$
Nickel-60	1.28 ± .08	0.0893g/^{2}	$0.971 \times 10^{21}/\text{cm}^2$

The number of target nuclei per unit area was found from the measured areal density of the targets, using

$$N_t = N_0\, \rho / A$$

where N_0 = Avogadro's number,

ρ = areal density × 1.082,

A = atomic weight.

The factor 1.082 was included because the targets were inclined $22\text{-}1/2^\circ$ to the incoming beam direction. Measured values of ρ and calculated values of N_t are given in Table II.

An average solid angle subtended by the detector was computed from the integral

$$\overline{\Delta\Omega} = \frac{A}{(r_2 - r_1)} \int_{r_1}^{r_2} \frac{dr}{r^2} = \frac{A}{r_1 r_2} ,$$

where the length of the bubble chamber is $(r_2 - r_1)$ and A is the cross-sectional area of the cylindrical volume utilized in the detection of proton recoils. No attenuation factor was included in this expression, since r_1 and r_2 are of similar magnitude, and the energy-dependent correction would be of the second order of smallness. For the geometry encountered in the experiment one has

$$\overline{\Delta\Omega} = 3.82 \times 10^{-4} \text{ steradian.}$$

A computational program for the 650-type computer was used to make the cross-section calculations because of the relative ease with which a table of energy-dependent correction factors could be included. A multiplier was constructed from the density data in Table III and from the numerical expression for Eq. (6). This factor, when multiplied by the chamber efficiency factors and the number of proton recoils observed within the energy range E, gave the neutron-production cross section directly. Statistical errors on these data points were determined simultaneously. The data input for this analysis program were track answer cards from the proton track-analysis program. Data from several separate runs of a target could be quickly combined by adjusting the multiplier to include the total beam current represented and then processing cards from each run in succession.

IV. RESULTS

A. Measurement of Neutrons From the $t(d, n)He^4$ Reaction

With the bubble chamber spectrometer located at 90° to the deuteron beam direction, neutrons of 14.06 Mev should be observed arising from the $t(d, n)He^4$ reaction,[22] if the Q value is 17.58 Mev. The experimentally determined spectrum is shown in Fig. 12 for the case in which a neutron collimator of 5/8-inch diameter was interposed between the target and the spectrometer. This curve has a measured width at half maximum of 1.5 Mev, and is based on the analysis of 612 proton-recoil tracks. The spectra arising with the use of a 7/8-inch collimator and without a collimator were found to be very similar; because a 5/8-inch collimator effectively restricted the entry of neutrons to the desired cylindrical region of the chamber, it was selected for use throughout the data-collection portion of the experiment. This reduced the accumulation of unwanted track data and allowed the neutron flux entering the chamber to be increased without giving rise to obscuring tracks in the photographs,thus providing a gain of about four in accepted tracks per roll of film analyzed.

In order to examine quantitatively this neutron-energy spectrum arising from the d-t reaction, it is necessary to consider both the energy spectrum of the incoming neutron flux and the effects introduced by the data-reduction technique. Because the peak in the d-t cross section occurs at low energy and the Q of the reaction is high, neutrons observed at 90° to the incoming deuteron beam have little spread in energy. However, if the deuterons have undergone significant Coulomb scattering within the target, the angle of neutron production may deviate from 90°. It is shown in Appendix C that consideration of the effects of multiple scattering of deuterons passing through the target of gold and tritium-titanium gives rise to a neutron-energy spectrum at 90° with the shape shown in Fig. 13. This curve has a full width at one-half maximum of 0.6 Mev.

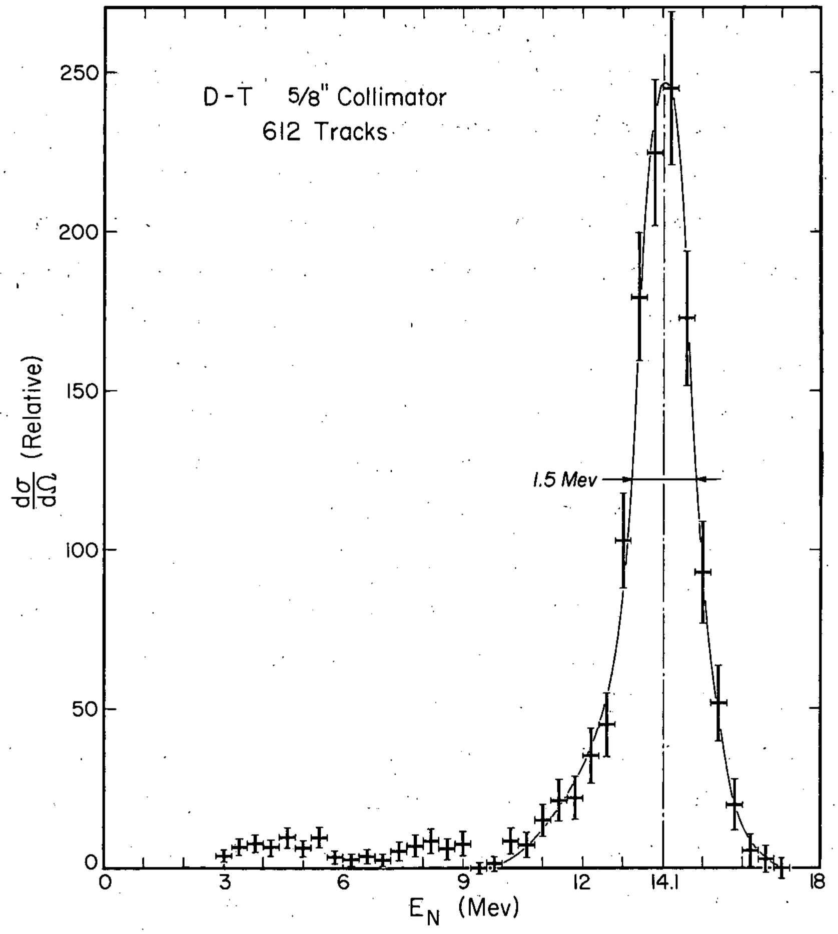

MU-14946

Fig. 12. Measured spectrum of neutrons from the t(d, n)He^4 reaction observed at 90°.

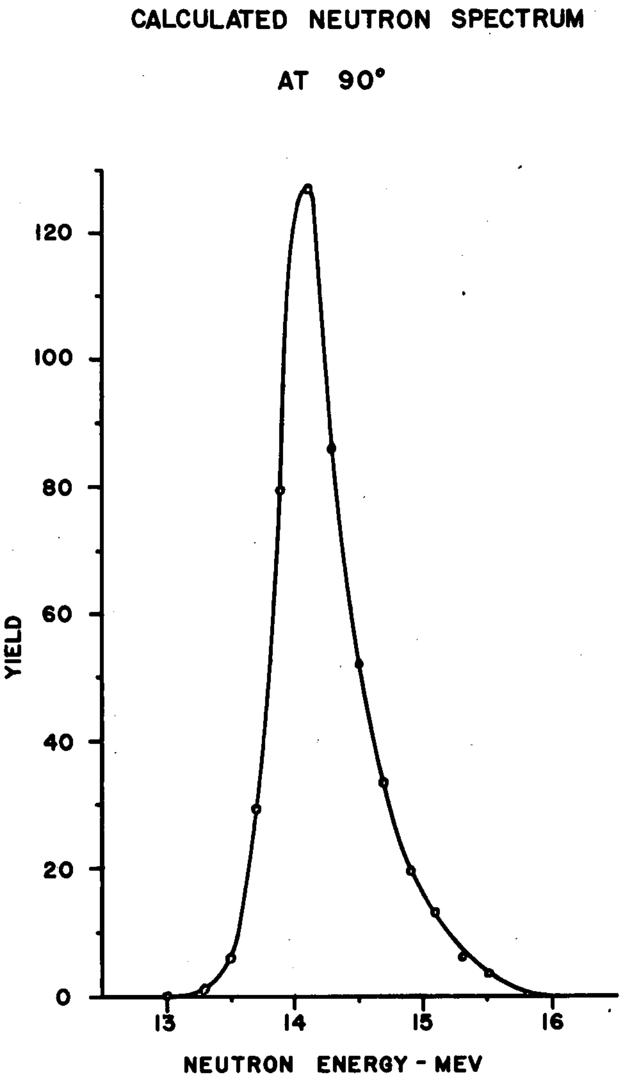

MU-16105

Fig. 13. Calculated neutron-energy spectrum at 90° due to multiple Coulomb scattering within the tritium target assembly.

Effects of measurement errors made during data accumulation were determined by having a selected portion of the d-t reaction photographs read by each reader. A total of 46 tracks was measured by each reader, and every person's results for each track were compared with the mean of all results for that track. Frequency plots of the deviations from the mean energy of each observer were found to have an average width at half-maximum amplitude of 0.2 Mev. Assuming that each of these curves may be represented by a Gaussian function with equivalent width, and letting

w = width of the d-t energy spectrum = 1.5 Mev,
w_c = width of a neutron spectrum shape due to multiple scattering = 0.6 Mev,
w_r = width of the reading error curve = 0.2 Mev,
w_i = width of the instrumental resolution curve,

one may write the over-all width of the energy spectrum

$$w^2 = w_c^2 + w_r^2 + w_i^2 ,$$

from which is found $w_i = 1.37$ Mev. The spread in the instrumental resolution curve is due to scattering of neutrons before they enter the bubble chamber and distortions in the proton recoil tracks as measured by the reading system. These effects cannot be separated directly.

B. Angular Distributions of Recoil Protons

Equation (4), Section III D, shows that the expected laboratory-system angular distribution of recoil protons arising from an isotropic distribution in the center-of-momentum system would be proportional to $\sin 2\theta_L$. Figure 14 shows the angular distribution of protons having energies between 5 and 25 Mev. These data were combined from nickel-58 and nickel-60 runs made with the bubble chamber at an angle of 53° to the bombarding proton beam. There are 2,074 protons with scattering angles less than 30° in the spectrum. These data are combined into 3° increments. A curve normalized to the total number of tracks in the range 0° to 30° is superimposed for comparison. At angles above 30° the spectrum is seen to fall below that which is expected; this is due

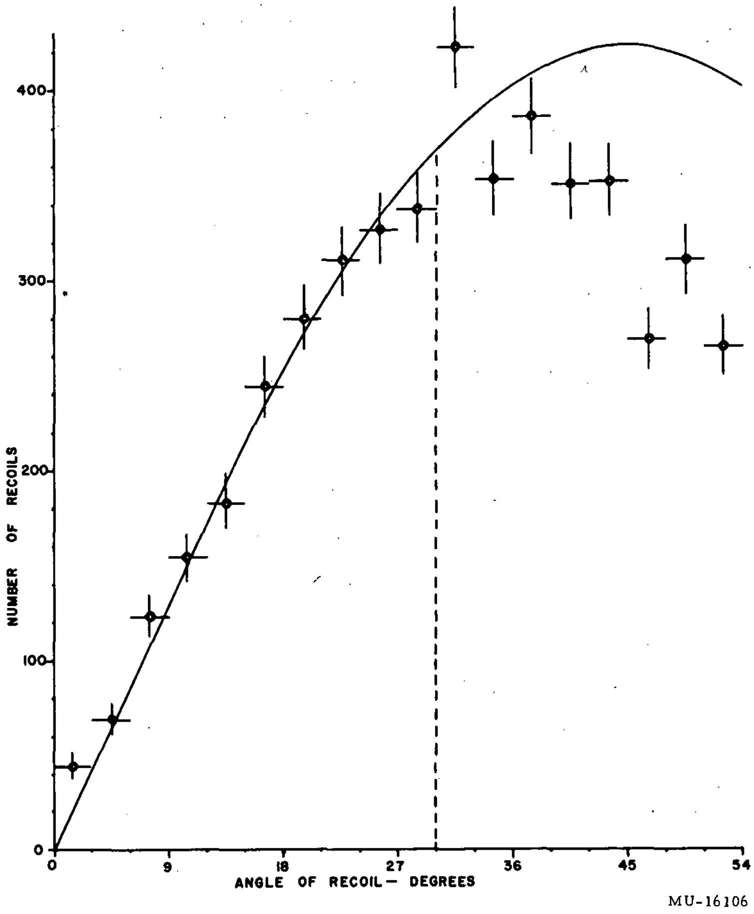

Fig. 14. Angular distribution of 2,074 recoil protons observed in the liquid hydrogen bubble chamber. The solid curve is a sin 2θ curve normalized to the total number of tracks within the interval $0^{\circ} \leq \theta \leq 30^{\circ}$.

to a low-energy cutoff in proton-recoil energies observed for neutron energies near 5 Mev. At 45^o a recoil proton from a 5-Mev neutron has an energy of 2.5 Mev, whereas the analysis program was prepared to accept only recoil tracks with energies above 3 Mev. With a maximum acceptance angle of 30^o the tracks near 5 Mev are totally included. Between 0^o and 30^o distortions due to the anisotropy of higher-energy n-p scattering are small; since the n-p scattering cross section decreases rapidly with energy and the experimentally observed neutron energies are concentrated toward low values, the effects of this anisotropy are greatly reduced and are not visible in Fig. 14.

C. Energy Spectra From Target Bombardments

Target-bombardment data processed with both the track-analysis program and the efficiency-correction and cross-section program were subsequently corrected for the stray background that entered the chamber from directions other than down the collimator. Background for each target at each angle was determined from runs taken with the collimator hole closed. A typical background spectrum is shown in Fig. 15; this case is for nickel-58 at 90^o. All the background results were found to be quite similar.

Cross sections for neutron production from 31.5-Mev proton bombardment are shown in Figs. 16 through 24. Here the cross section for producing a neutron within a unit energy interval is given as a function of neutron energy for each spectrometer position. The number of recoil proton tracks represented in each spectrum is shown in Table IV.

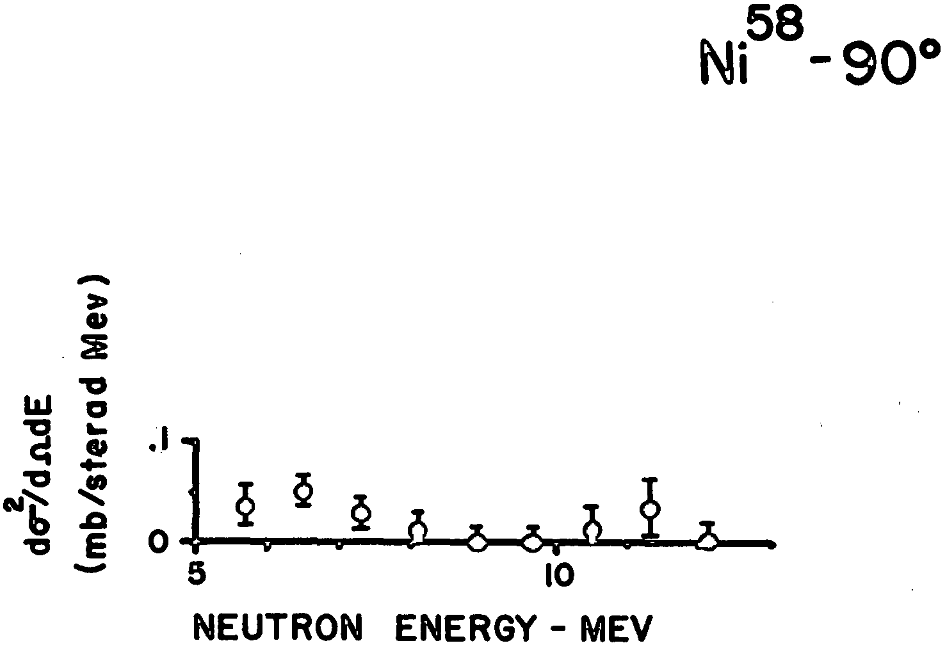

MU-16107

Fig. 15. Spectrum of background neutrons measured for Ni^{58} as determined from closed-collimator data. This relative magnitude was typical of all targets and angles of observation.

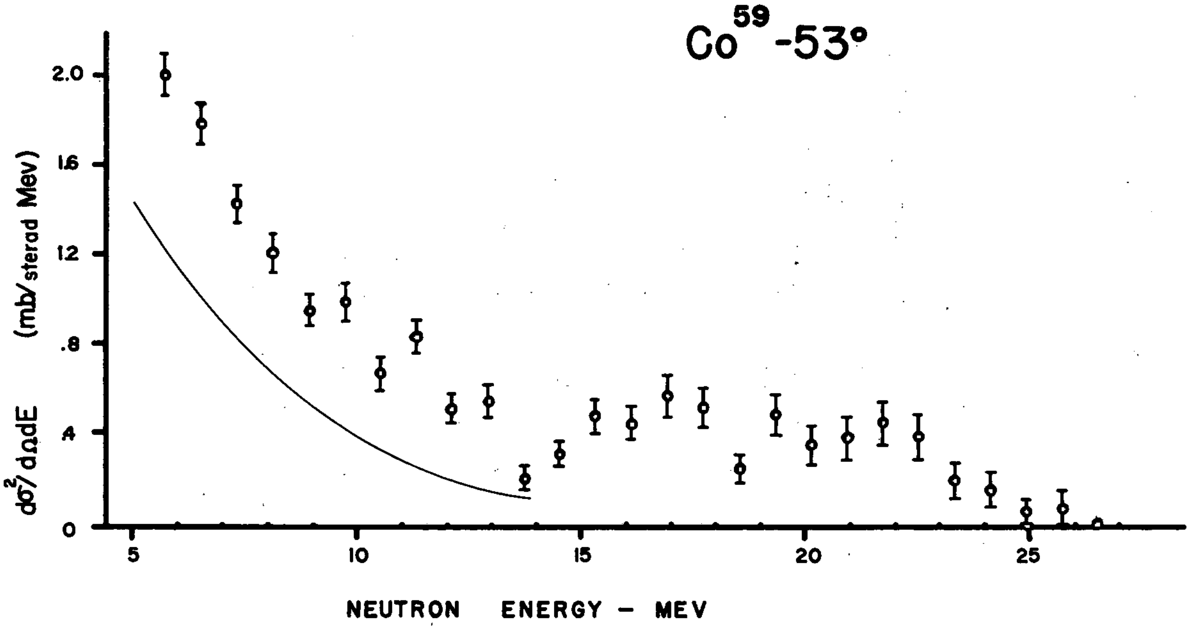

MU-16108

Fig. 16. Differential cross section for the production of neutrons at 53° by bombarding Co^{59} with 31.5-Mev protons. Errors are statistical probable errors. Solid curve is a fit of an evaporation spectrum to the 127° data.

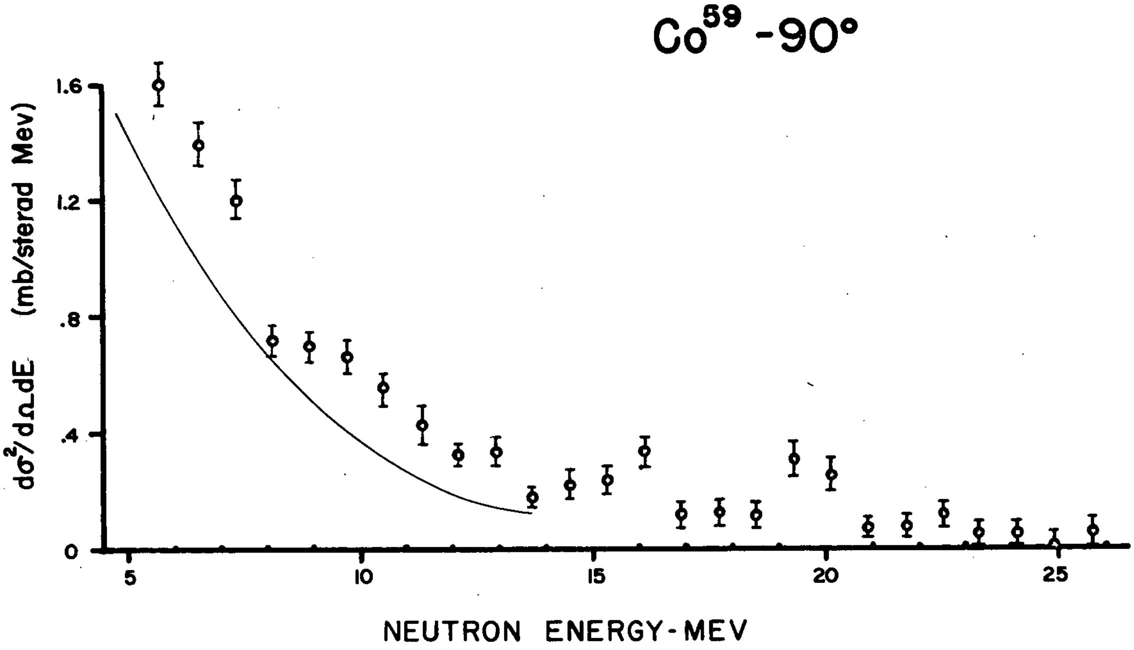

MU-16109

Fig. 17. Differential cross section for the production of neutrons at 90° by bombarding Co^{59} with 31.5-Mev protons. Errors are statistical probable errors. Solid curve is a fit of an evaporation spectrum to 127° data.

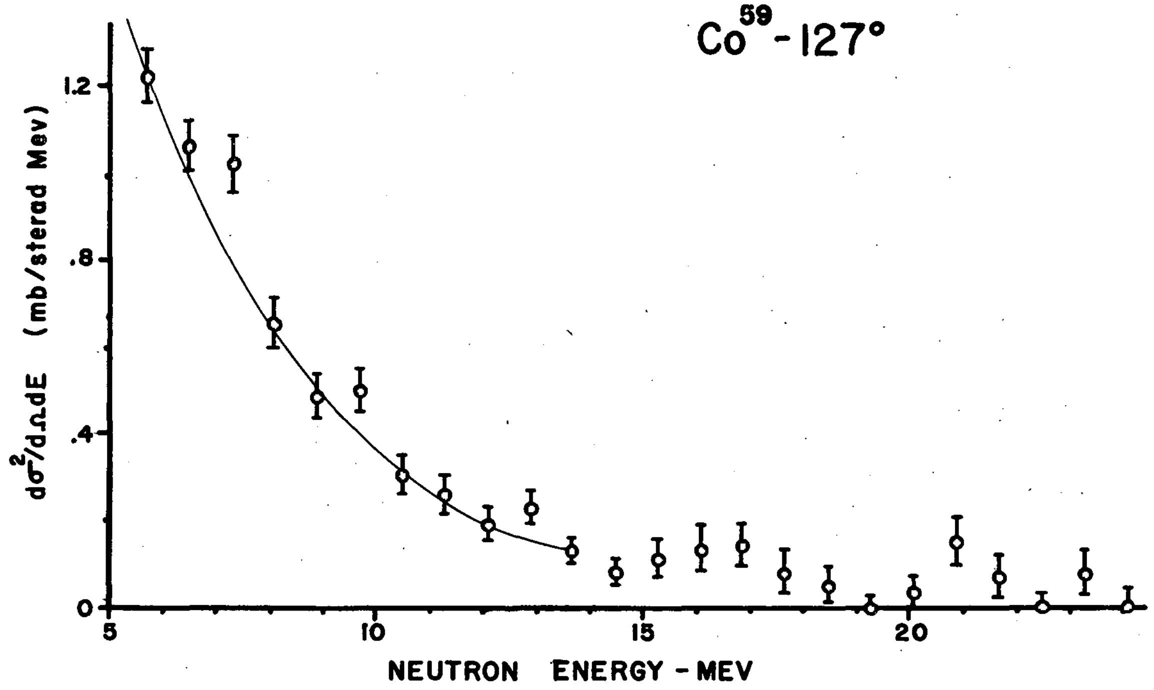

MU-16110

Fig. 18. Differential cross section for the production of neutrons at 127° by bombarding Co^{59} with 31.5-Mev protons. Errors are statistical probable errors. Solid curve is a fit of an evaporation spectrum.

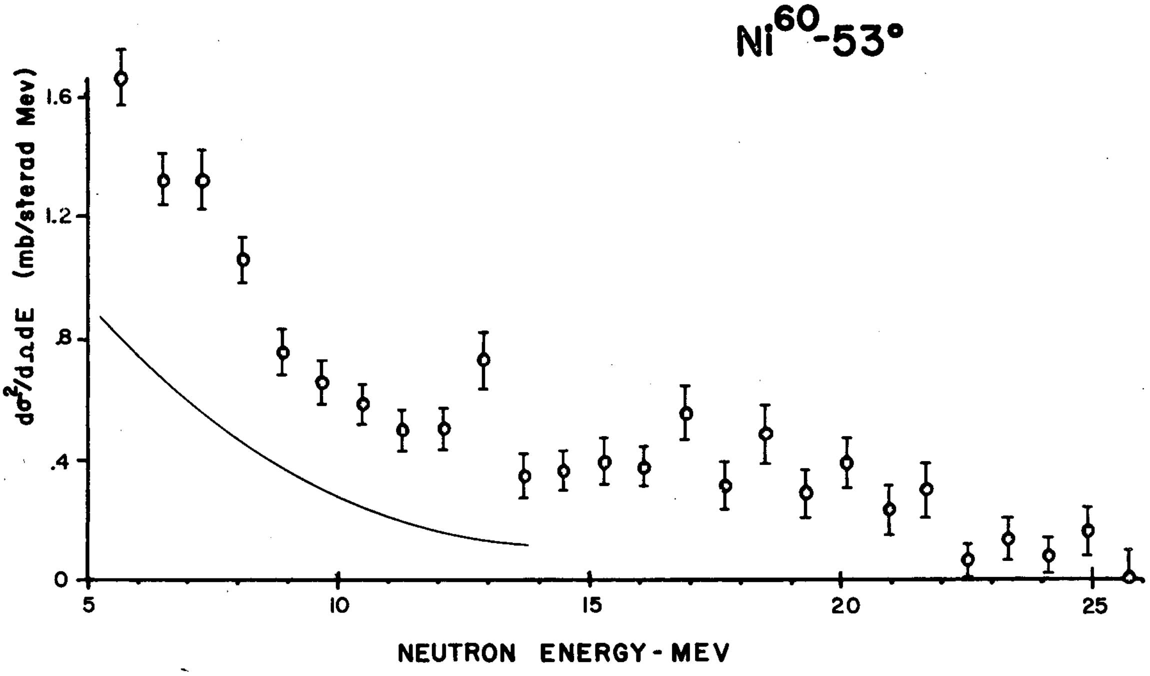

MU-16111

Fig. 19. Differential cross section for the production of neutrons at 53° by bombarding Ni^{60} with 31.5-Mev protons. Errors are statistical probable errors. Solid curve is a fit of an evaporation spectrum to 127° data.

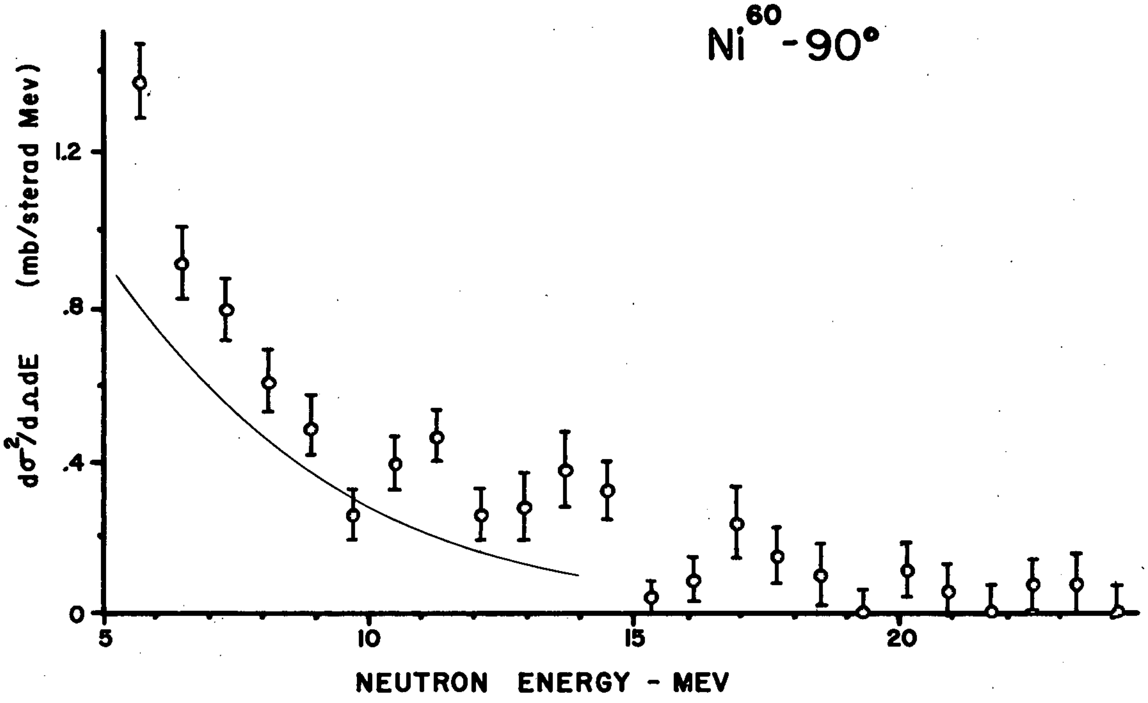

MU-16112

Fig. 20. Differential cross section for the production of neutrons at 90° by bombarding Ni^{60} with 31.5-Mev protons. Errors are statistical probable errors. Solid curve is a fit of an evaporation spectrum to the 127° data.

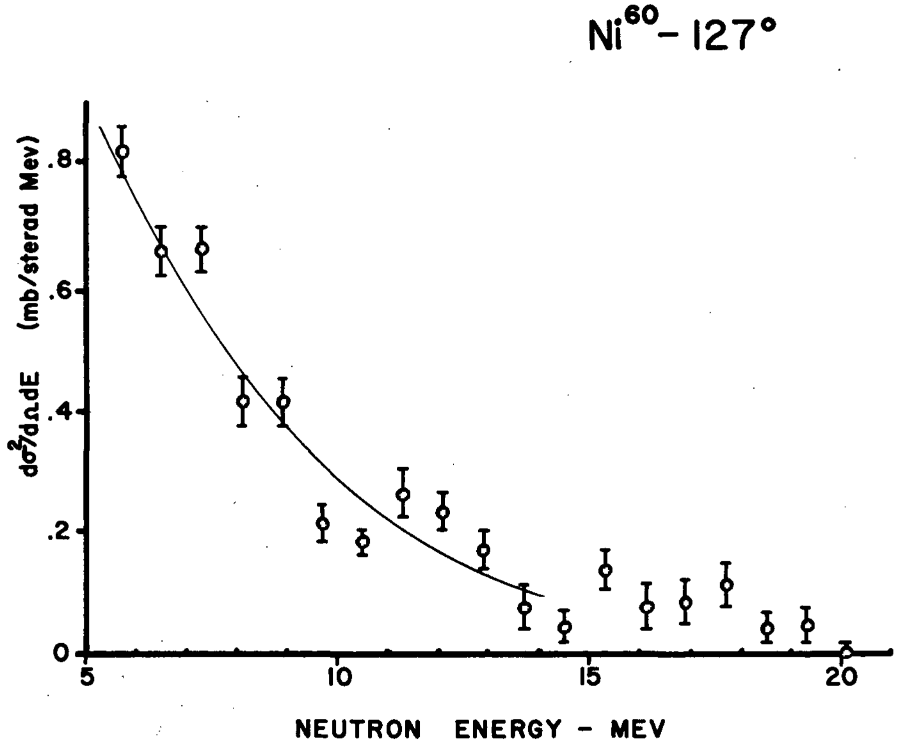

MU-16113

Fig. 21. Differential cross section for the production of neutrons at 127° by bombarding Ni^{60} with 31.5-Mev protons. Errors are statistical probable errors. Solid curve is a fit of an evaporation spectrum.

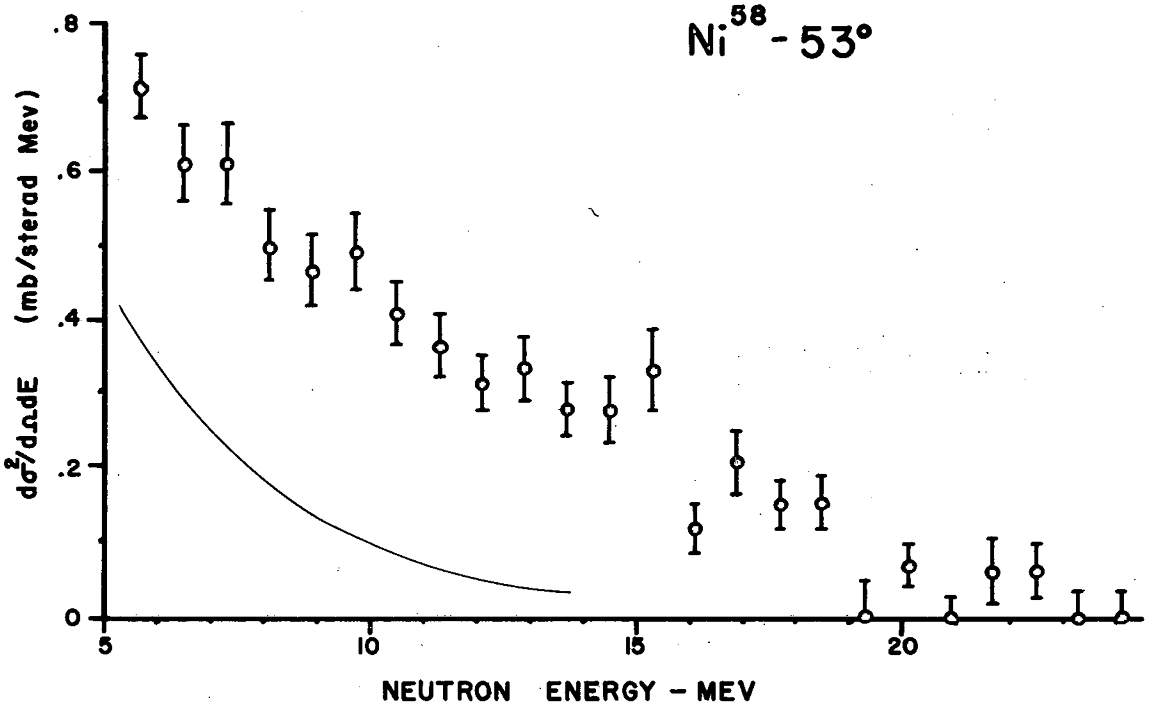

MU-16114

Fig. 22. Differential cross section for the production of neutrons at 53° by bombarding Ni^{58} with 31.5-Mev protons. Errors are statistical probable errors. Solid curve is a fit of an evaporation spectrum to 127° data.

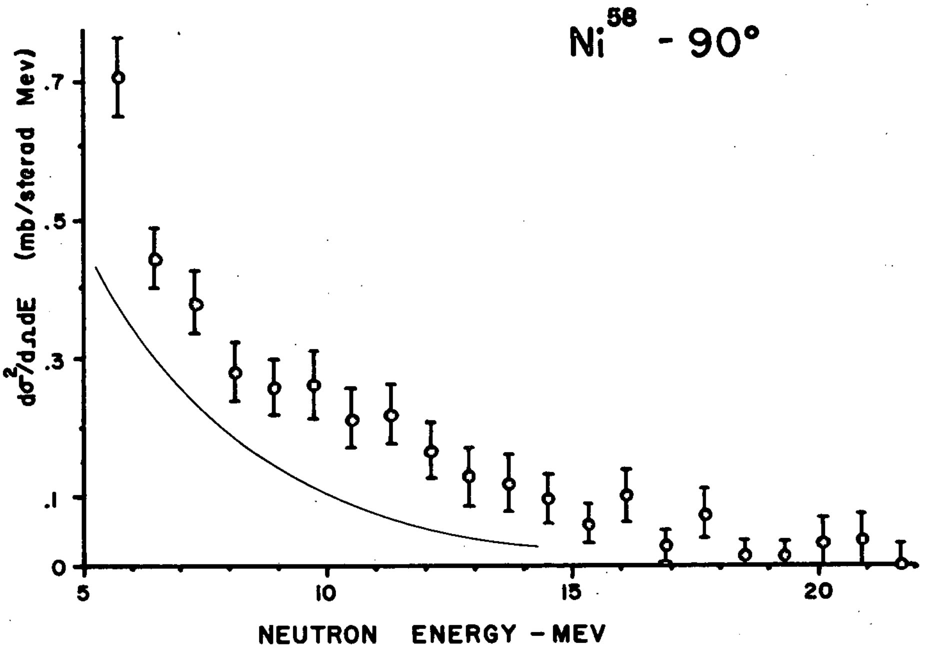

MU-16115

Fig. 23. Differential cross section for the production of neutrons at 90° by bombarding Ni^{58} with 31.5-Mev protons. Errors are statistical probable errors. Solid curve is a fit of an evaporation spectrum to the 127° data.

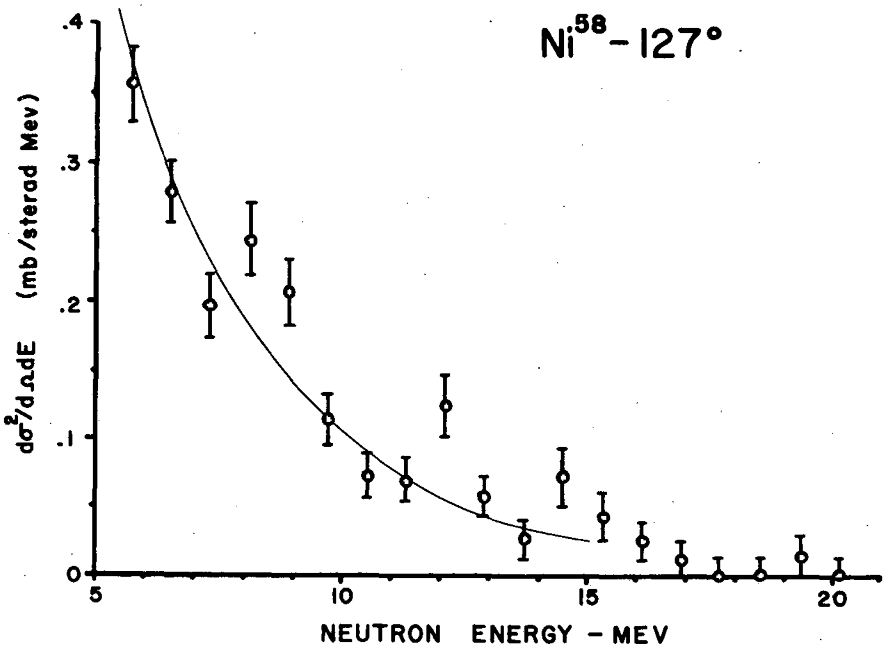

MU-16116

Fig. 24. Differential cross section for the production of neutrons at 127° by bombarding Ni^{58} with 31.5-Mev protons. Errors are statistical probable errors. Solid curve is a fit of an evaporation spectrum.

Table IV

Numbers of recoil-proton tracks in spectra at various angles

	Angle		
Target	53°	90°	127°
Co^{59}	1698	1510	1229
Ni^{60}	1278	617	1161
Ni^{58}	1062	979	592

Each datum represents a combination of neutron energies lying within an energy range of 0.8 Mev. The errors shown are statistical only. Uncertainties in relative cross sections for a single target depend only on these statistical errors; calculation of relative cross sections among the three targets depends on knowledge of the target properties and the relative collection ratios of beam charge. These may be estimated from Table III to be less than 10%.

In order to facilitate visual comparisons of data between pairs of targets, the energy spectra are shown in Figs. 25 through 27 with cobalt-59 and nickel-60 plotted together and in Figures 28 through 30 with nickel-58 and nickel-60 plotted together. The probable errors are again not shown, so as to avoid confusion due to overlap. Areas under the cross-section-curves were measured with a polar planimeter and the cross sections for several energy intervals are shown in Table V. In addition , in Figs. 31 through 33 the data are replotted to show the character of the angular dependence for each target. Again the probable errors are omitted.

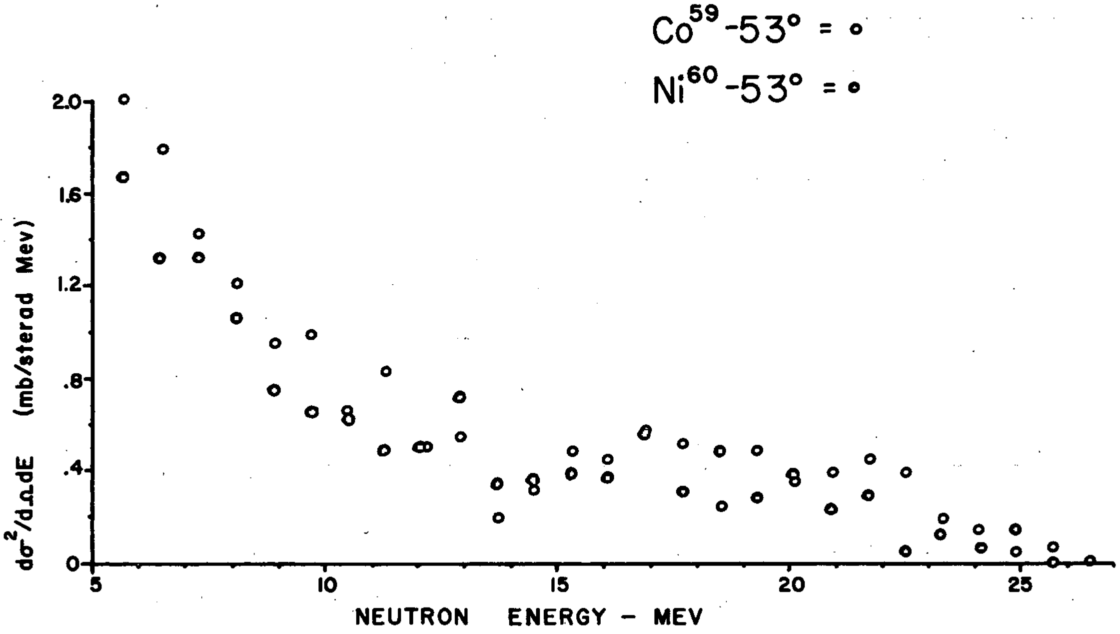

MU-16117

Fig. 25. Comparison of differential cross sections of Co^{59} and Ni^{60} for neutron production at 53°. Errors are the same as in Figs. 16 and 19 and are not shown.

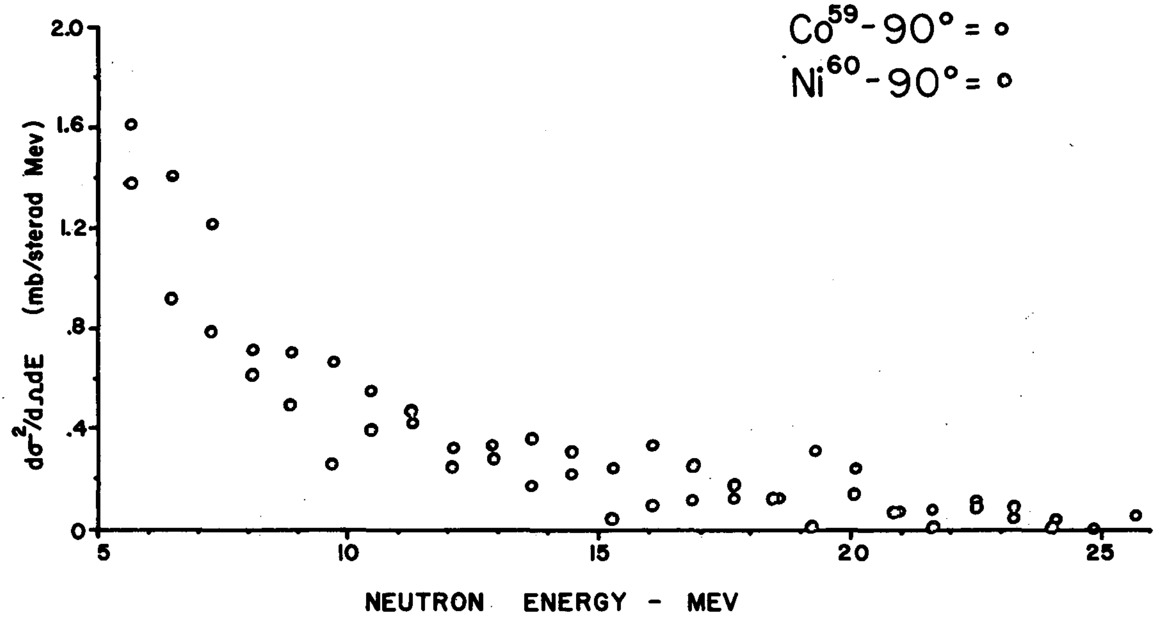

MU-16118

Fig. 26. Comparison of differential cross sections of Co^{59} and Ni^{60} for neutron production at 90°. Errors are the same as in Figs. 17 and 20 and are not shown.

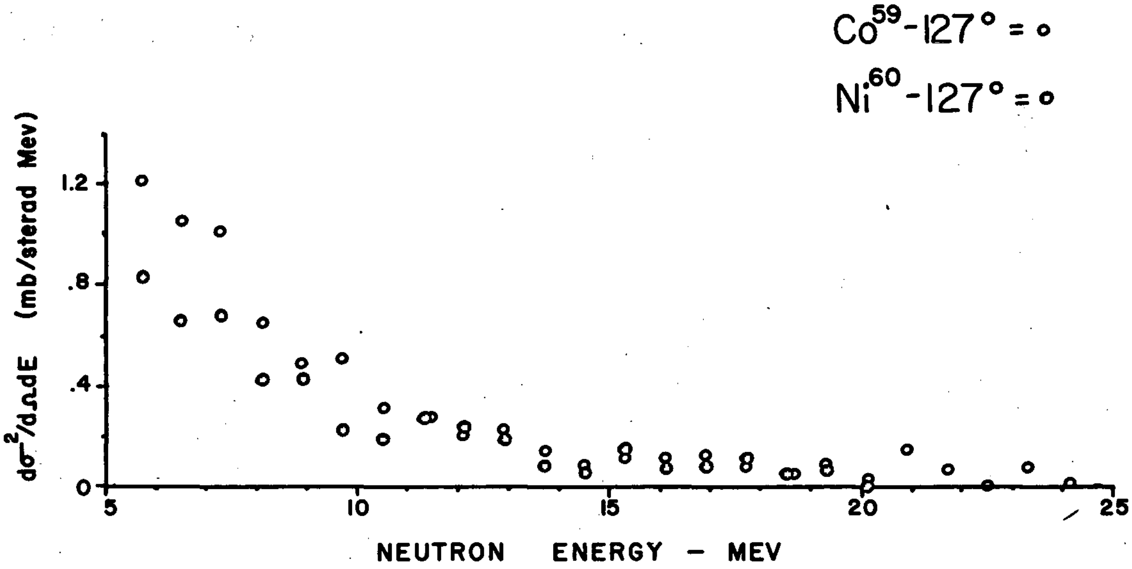

MU-16119

Fig. 27. Comparison of differential cross sections of Co^{59} and Ni^{60} for neutron production at 127°. Errors are the same as in Figs. 18 and 21 and are not shown.

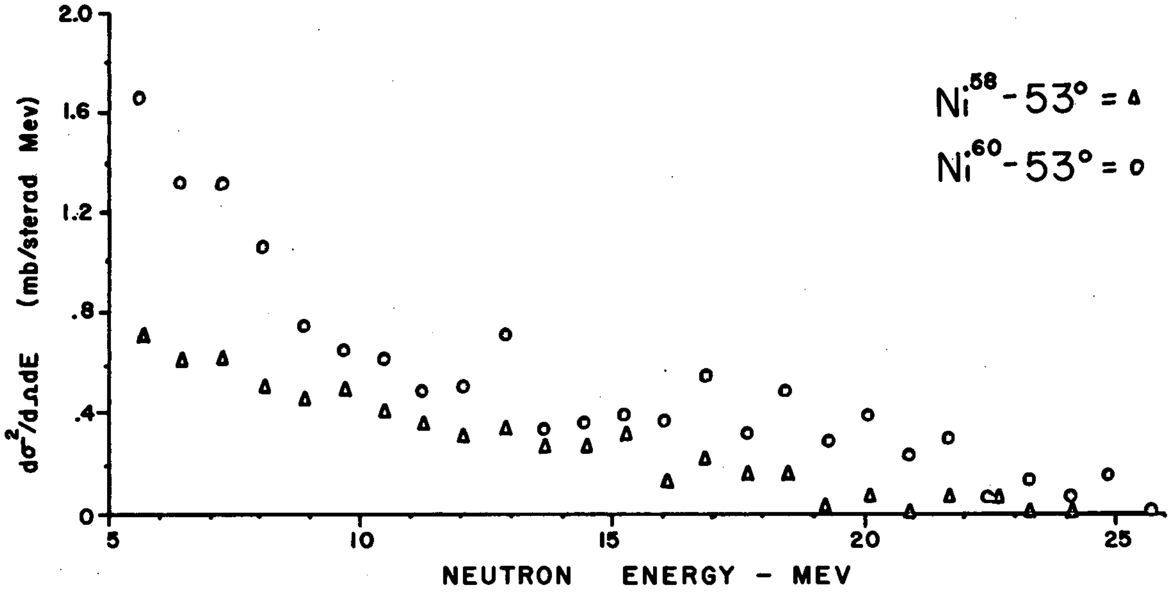

MU-16120

Fig. 28. Comparison of differential cross sections of Ni^{58} and Ni^{60} for neutron production at 53°. Errors are the same as in Figs. 19 and 22 and are not shown.

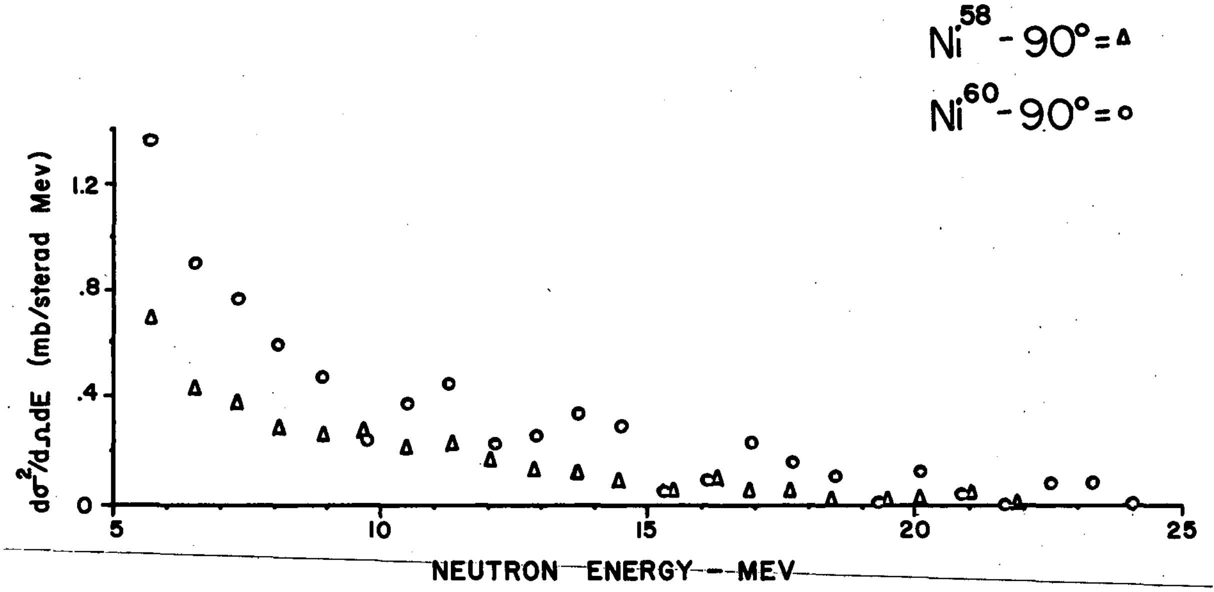

MU-16121

Fig. 29. Comparison of differential cross sections of Ni^{58} and Ni^{60} for neutron production at 90°. Errors are the same as in Figs. 20 and 23 and are not shown.

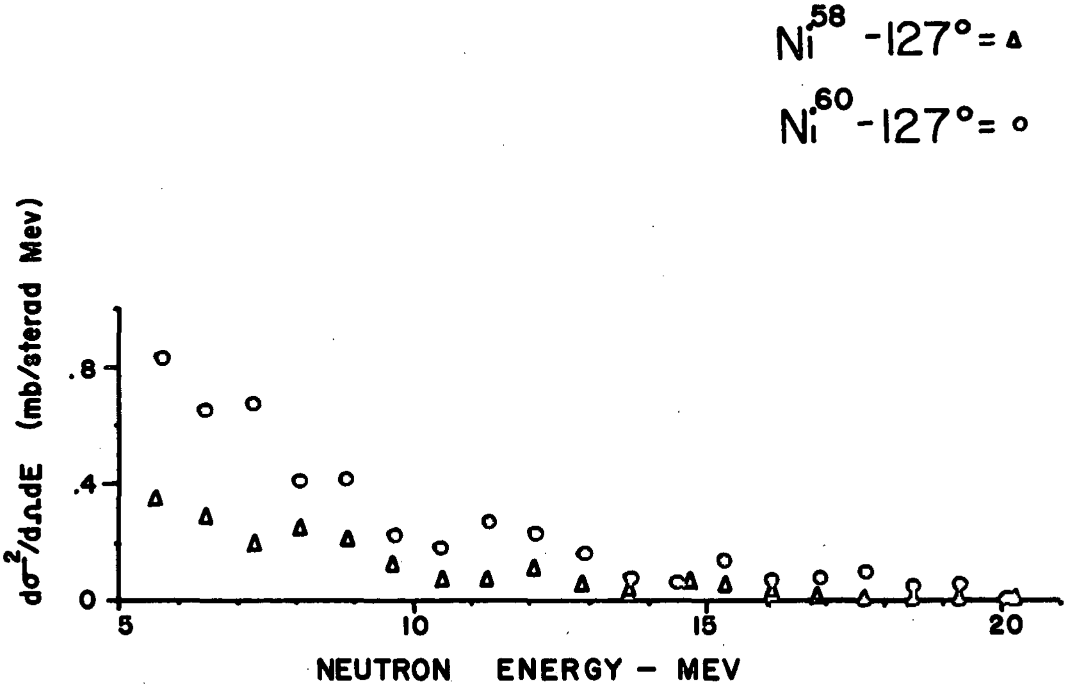

MU-16122

Fig. 30. Comparison of differential cross sections of Ni^{58} and Ni^{60} for neutron production at 127°. Errors are the same as in Figs. 21 and 24 and are not shown.

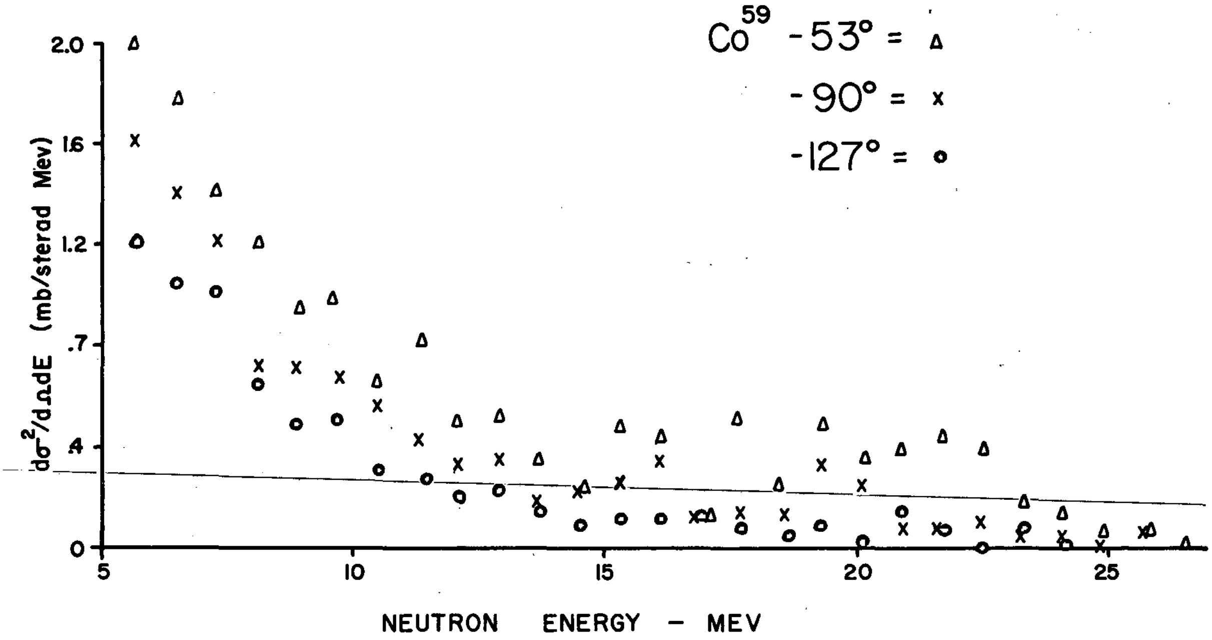

MU-16123

Fig. 31. Comparison of the differential cross sections for neutron production in Co^{59} at 53°, 90°, and 127°. Statistical errors have not been shown.

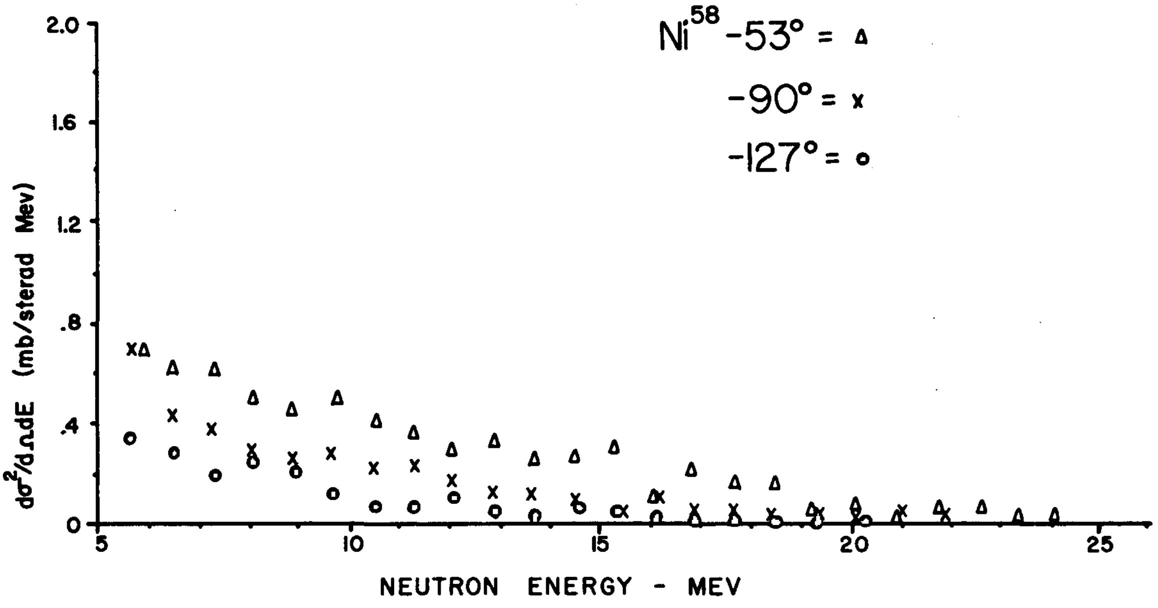

MU-16124

Fig. 32. Comparison of the differential cross sections for neutron production in Ni^{58} at 53°, 90°, and 127°. Statistical errors have not been shown.

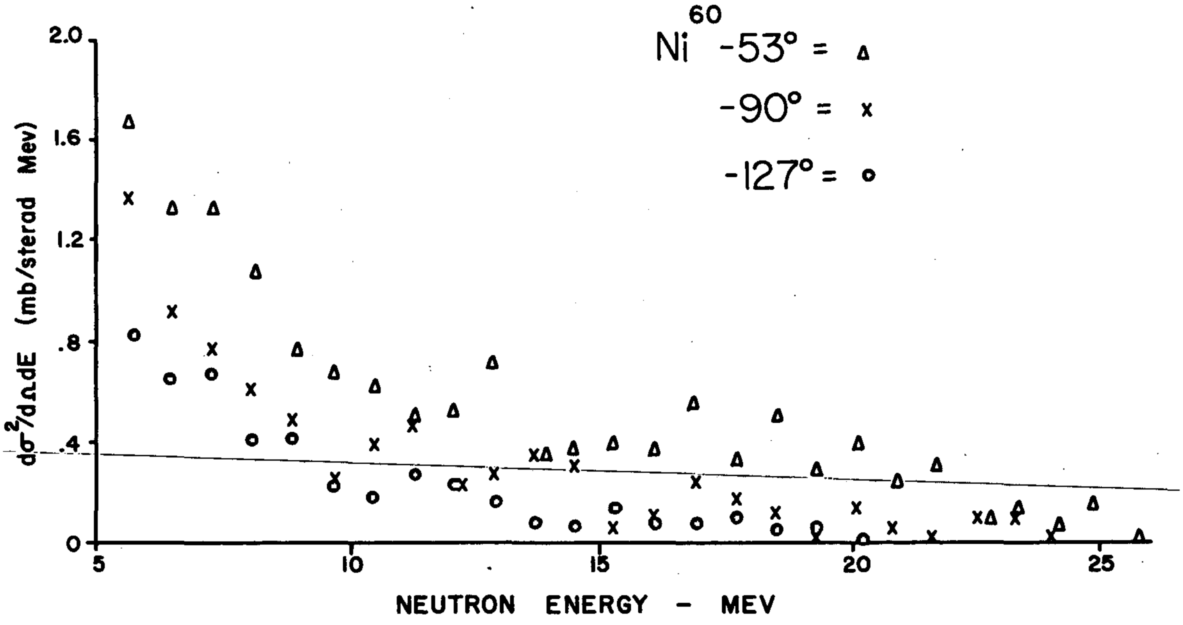

MU-16125

Fig. 33. Comparison of the differential cross section for neutron production in Ni^{60} at 53°, 90°, and 127°. Statistical errors have not been shown.

Table V

Cross sections
(mb/sterad)

Energy range (Mev)	Ni^{58} 53^6	Ni^{58} 90^o	Ni^{58} 127^o	Ni^{60} 53^o	Ni^{60} 90^o	Ni^{60} 127^o	Co^{59} 53^o	Co^{59} 90^o	Co^{59} 127^o
6-8	1.63	1.00	0.67	3.22	2.22	1.54	3.80	2.94	2.66
8-10	1.30	0.69	0.48	1.93	1.07	0.83	2.47	1.60	1.41
10-12	1.02	0.54	0.22	1.24	1.01	0.57	1.83	1.16	0.78
12-15	1.20	0.49	0.27	1.75	1.15	0.42	1.39	0.90	0.63
15-20	1.09	0.37	0.12	2.46	0.67	0.48	2.82	1.25	0.59
20-25	0.21	0.07	--	1.15	0.34	--	1.88	0.55	0.32

Target	6-10 Mev angle 53^o	6-10 Mev angle 90^o	6-10 Mev angle 127^o	Above 10 Mev 53^o	Above 10 Mev 90^o	Above 10 Mev 127^o
Ni^{58}	2.93	1.69	1.15	3.52	1.47	0.62
Ni^{60}	5.15	3.29	2.37	6.60	3.17	1.47
Co^{59}	6.27	4.54	4.07	7.92	3.86	2.32

V. DISCUSSION OF RESULTS

A. Angular Distributions

Throughout the energy range covered by the available data from each target, it can be seen from Figs. 31 through 33 that the neutron flux is more intense in the forward hemisphere than it is in the backward hemisphere. The asymmetry increases with energy until, for both nickel-58 and nickel-60, the component above 20 Mev becomes vanishingly small at 127°. In Co^{59}, however, there remains a significant contribution above 20 Mev. Because of the asymmetry present in the angular dependence of neutron yields, reactions in addition to those proceeding through the formation and statistical decay of a compound nuclear system should be present. An estimate of the contribution of compound-nuclear processes has been made by assuming that the spectra observed at 127° are primarily composed of neutrons from these reactions. According to the formulation by Weisskopf,[6] the neutron-energy spectrum would be expected to obey a relation of the form

$$I_n(E_n)dE_n = AE_n\sigma_c(E_n)\exp(-E_n/T)dE_n, \qquad (7)$$

where E_n is the neutron kinetic energy. Here $\sigma_c(E_n)$ is the cross section for formation of the compound nucleus by neutrons having energy E_n (in an inverse reaction), and T is a parameter, usually called the nuclear temperature, appropriate to the excitation energy of the residual nucleus.

With the aid of the table for $\sigma_c(E)/\pi R^2$ given by Blatt and Weisskopf for neutrons,[6] the quantity

$$\frac{d^2\sigma}{d\Omega dE} \Big/ \frac{E_n\sigma}{\pi R^2}$$

is plotted against neutron energy E_n on a semilogarithmic scale in Figs. 34 through 36. This quantity should give rise to a straight line if the Weisskopf expression is obeyed. The negative reciprocal slope of the line is then proportional to the parameter T.

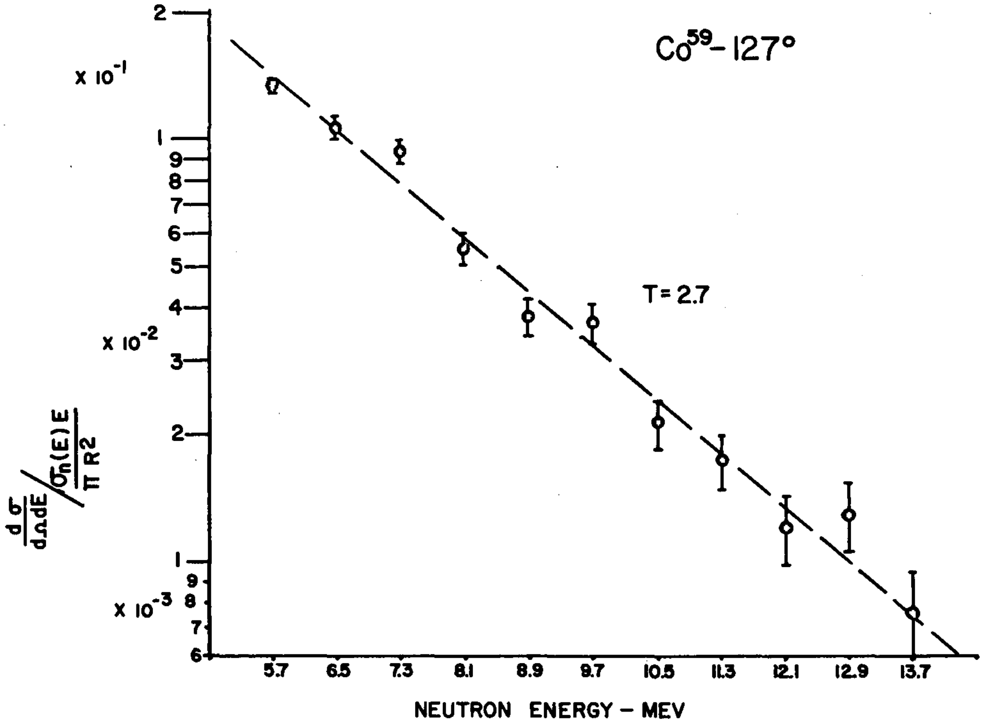

MU-16126

Fig. 34. Ln $\frac{d^2\sigma/d\Omega dE}{E_n\sigma_c/\pi R^2}$ vs. neutron energy for Co^{59}; 127° data.

Values for $\sigma_c/\pi R^2$ were taken from Blatt and Weisskopf,[6] using a value of $R = 1.3\times 10^{-13} A^{1/3}$ cm. Errors shown are statistical probable errors.

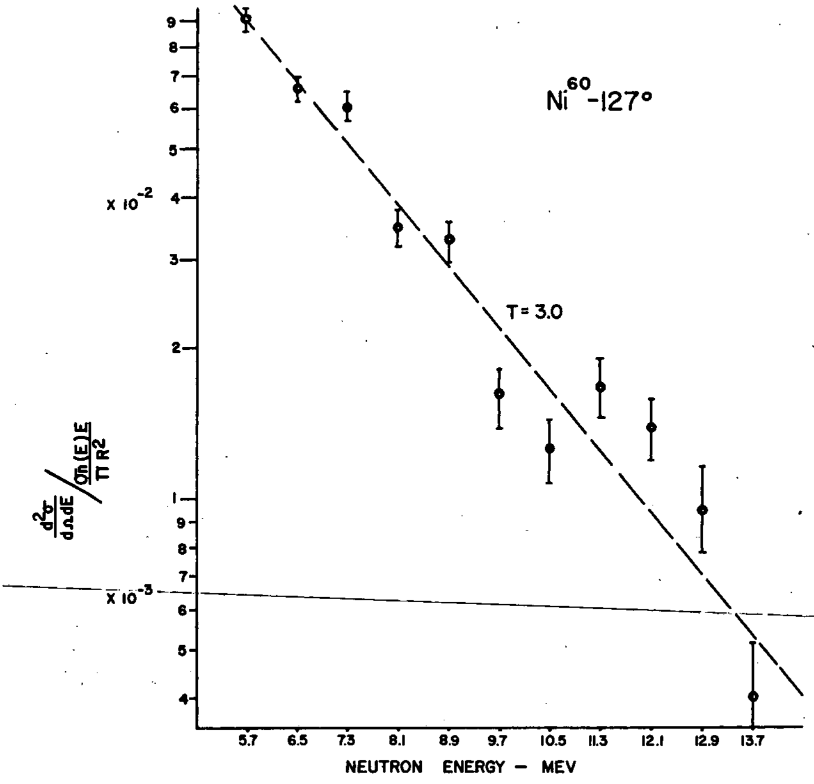

MU-16127

Fig. 35. Ln $\frac{d^2\sigma/d\Omega dE}{E_n\sigma_c/\pi R^2}$ vs. neutron energy for Ni^{60}; 127° data. Values for $\sigma_c/\pi R^2$ were taken from Blatt and Weisskopf,[6] using a value of $R = 1.3\times 10^{-13}\ A^{1/3}$ cm. Errors shown are statistical probable errors.

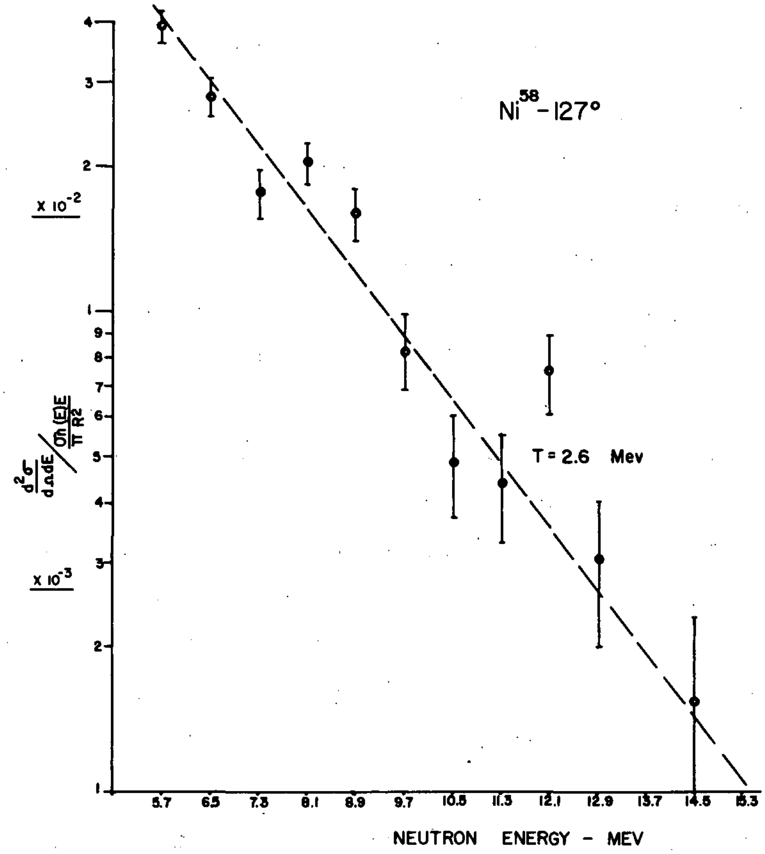

MU-16128

Fig. 36. Ln $\frac{d^2\sigma/d\Omega dE}{E_n\sigma_c/\pi R^2}$ vs. neutron energy for Ni^{58}; 127° data. Values for $\sigma_c/\pi R^2$ were taken from Blatt and Weisskopf,[6] using a value of $R = 1.3 \times 10^{-13}\ A^{1/3}$cm. Errors shown are statistical probable errors.

The values of T for each target at 127° were found to be

Co^{59}: T = 2.7 Mev,
Ni^{58}: T = 2.6 Mev,
Ni^{60}: T = 3.0 Mev.

By use of these values for T, Eq. (7) was fitted to the 127° neutron-spectra plots, shown by the solid curves in Figs. 18, 21, and 24. These curves reproduce the data trend up to energies of about 13 Mev. These "evaporation spectra" curves are also reproduced on the 53° and 90° spectra on the basis of an assumption of isotropic emission in the laboratory system. It can be shown that motion of the center of momentum of the projectile-target system cannot account for the observed anisotropy, for the momentum transfer required would be of the order of four times the incoming proton momentum. Furthermore, the velocity required to give rise to the observed anisotropy is not constant, but depends upon the energy region of the spectrum being treated.

The angular dependence of neutrons above 20 Mev is of special interest because of the reaction thresholds involved. Computed reaction Q values and neutron thresholds for 31.5-Mev proton bombardment are listed below.

Reaction	Q value (Mev)	Reference	Maximum neutron energy (Mev)
$Co^{59}(p,n)Ni^{59}$	-1.86	Quisenberry et al.(25)	29.6
$Co^{59}(p,pn)Co^{58}$	-10.49	Quisenberry et al.	20.8
$Co^{59}(p,2n)Ni^{58}$	-10.87	Quisenberry et al.	20.5
$Ni^{60}(p,n)Cu^{60}$	-7.05	Quisenberry et al.	24.3
$Ni^{60}(p,pn)Ni^{59}$	-11.3	Quisenberry et al.	20.0
$Ni^{60}(p,2n)Cu^{59}$	-21.7[d]	Riddell(26)	9.5
$Ni^{58}(p,n)Cu^{58}$	-8.7	Wapstra(27)	22.7
$Ni^{58}(p,pn)Ni^{57}$	-11.76	Quisenberry et al.	19.7
$Ni^{58}(p,2n)Cu^{58}$	-20.6	Cohen(28)	10.7

[d] Computed from empirical atomic-mass table, by use of formula of Levy.[29]

Above 20.5 Mev, all neutrons from the nickel targets arise from (p, n) reactions. Examination of Figs. 21 and 24 shows that there is no contribution above 20 Mev in the backward angle for the nickel isotopes. This result is consistent with the assumption that these (p, n) reaction neutrons have arisen through interactions near the nuclear surface as suggested by Butler,[10] and hence possess the characteristic strong forward peaking expected on the basis of this description. The less extreme peaking for Co^{59} could indicate the presence of states involving the acceptance of more angular momentum by the target nucleus than in the nickel isotopes. Evidently the vacant proton state in the 1 f 7/2 shell enhances the p, n cross section, as evidenced by the differences in the Ni^{60} and Co^{59} spectra above 20 Mev.

B. Yield

With reference to Figs. 28 through 30, it is evident that the differential cross sections for neutron production in Ni^{58} are significantly smaller than in Ni^{60} at all angles of observation. For energies above 12 Mev there seems to be a ratio of about 1:2 between the neutron yields. The yields from Co^{59} and Ni^{60} are more comparable, with evidently a somewhat greater yield from Co^{59} at all angles. It would seem attractive to postulate that, within the energy range where (p, pn) reactions might proceed with relatively little interaction with the remainder of the nucleus, there is a correlation between the neutron shell-occupation number and observed neutron yield.

An estimate of the total neutron-emission spectrum for each target was made to allow a comparison of the shape and yield with predictions of the evaporation theory. The estimation was made by replacing the integral expression

$$\frac{d\sigma}{dE} = \int \frac{d^2\sigma}{d\Omega dE} \, d\Omega$$

by the sum

$$\frac{d\sigma}{dE} \cong 2\pi \sum_{i=1}^{5} \left. \frac{d\sigma}{d\Omega dE} \right|_{\theta_i} \sin \theta_i \, \Delta\theta_i \, , \qquad (8)$$

with a 17° forward angle and a 163° backward angle included with the 53°, 90°, and 127° experimental observations. Cross sections at 17° were obtained by extrapolating the average angular dependence of the observed cross sections. It was assumed that the cross sections beyond 127° held constant. Neither of these assumptions unduly influences the result, because of the smallness of the solid-angle factor in each case. The estimated total emission spectra are shown in Figs. 37 through 39. These data were also plotted logarithmically in order to determine the corresponding values of the "temperature" parameter. A fit with a straight line was possible in each case, but considerable variation in the temperature resulted, as is shown below.

Co^{59}	T = 3.0 Mev
Ni^{60}	T = 3.4 Mev
Ni^{58}	T = 4.1 Mev

The magnitude and shape of the estimated yield spectra were compared with predictions made on the basis of the theory of evaporation of a compound nucleus. The formulation due to LeCouteur[30] provided a convenient framework in which to calculate emission probabilities for protons and neutrons from a given excited nucleus. The ratio of proton- to neutron-emission probabilities may be written

$$\frac{P_p}{P_n} = \left(\frac{R_p}{R_n}\right)^{1/4} \frac{a_n}{a_p} \exp 2\left[(a_p R_p)^{1/2} - (a_n R_n)^{1/2}\right], \quad (9)$$

with $R_i = E - (Q_i + V_i)$ = the maximum value of excitation of the residual nucleus when a particle of type i is emitted (i=p or n here),

Q_i = separation energy for particle i,

V_i = "corrected" Coulomb barrier for particle i,

a_i defined from the level-density formula $\rho(E) = Ce^{2(a_iE)^{1/2}}$,

E = excitation energy of the compound nucleus.

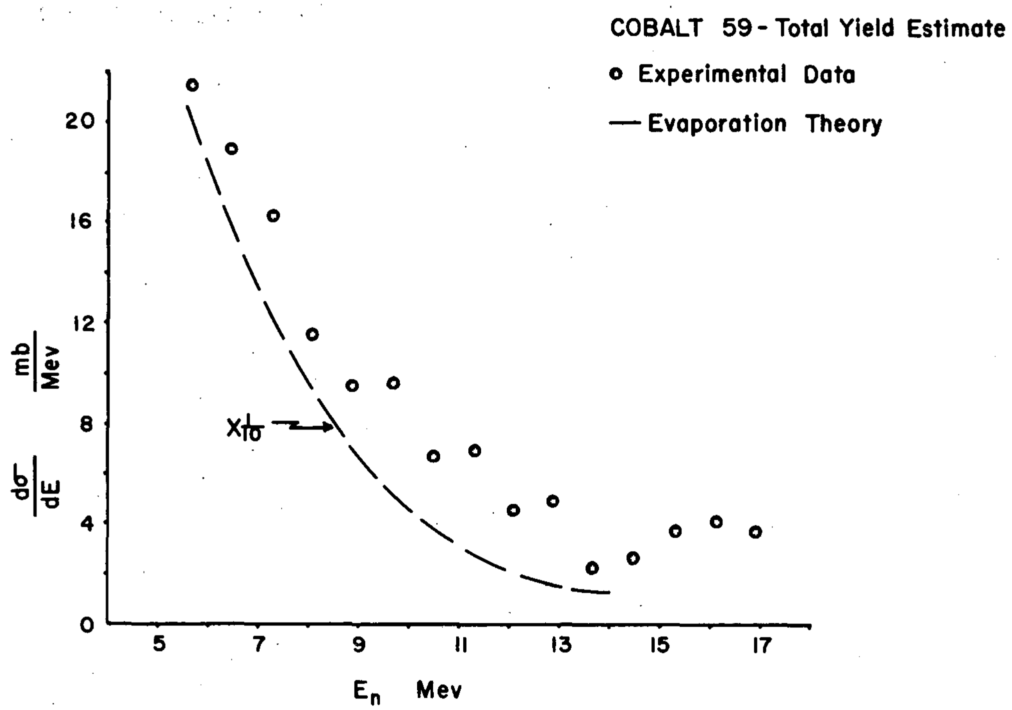

MU-16129

Fig. 37. Total neutron-emission spectrum of Co^{59} estimated from observations made at 53°, 90°, and 127°. The dashed curve is a prediction based on the theory of particle evaporation from an excited compound nucleus and is plotted with the vertical scale reduced by a factor of 10.

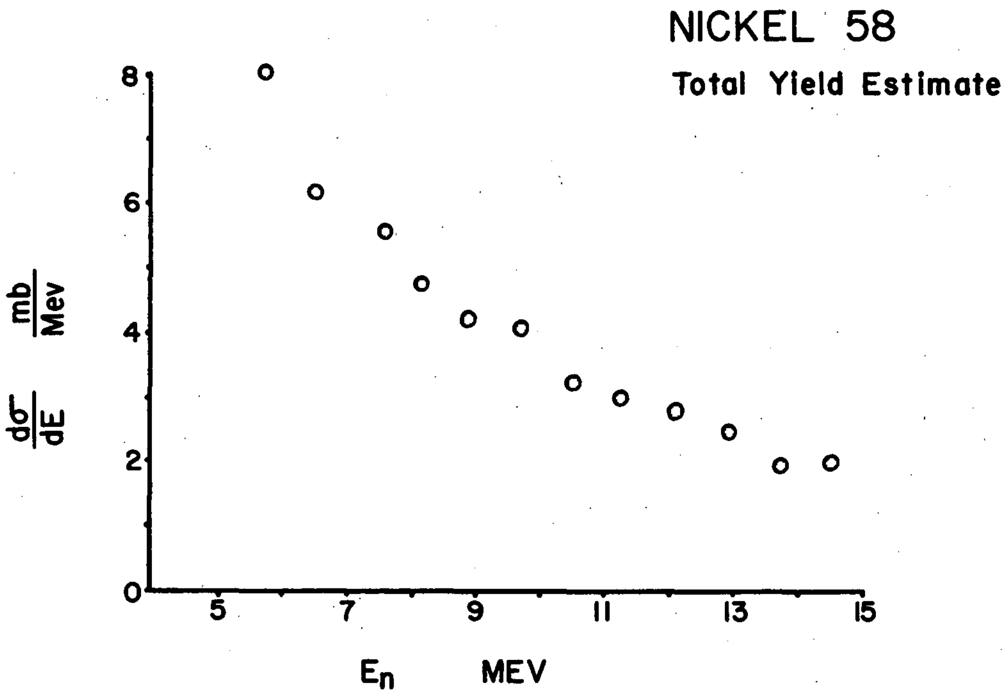

MU-16130

Fig. 38. Total neutron-emission spectrum of Ni^{58} estimated from observations made at 53°, 90°, and 127°.

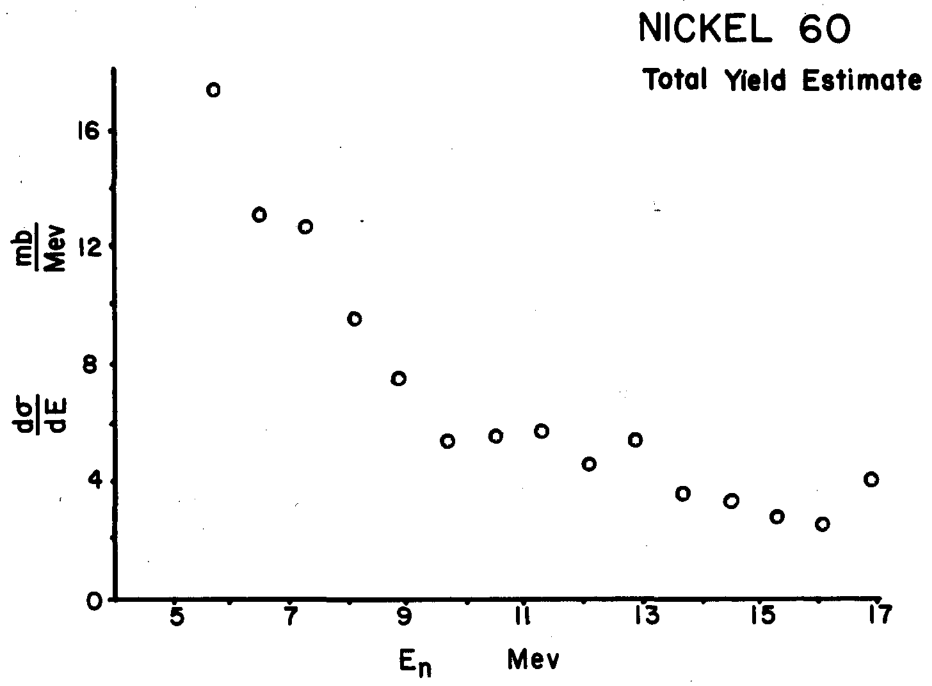

MU-16131

Fig. 39. Total neutron-emission spectrum of Ni^{60} estimated from observations made at 53°, 90°, and 127°.

The values used for V_i and a_i may be subject to considerable variation and exert much influence on the emission ratios. The Coulomb-barrier term was reduced to account for penetration effects by multiplying the factor $\frac{Ze^2}{R}$ by 0.7. The dependence of a_i on the neutron excess of the nucleus under consideration was taken to be that suggested by LeCouteur,

$$a_p^{1/2} = a^{1/2}(1-1.3\frac{\theta}{A}),$$

$$a_n^{1/2} = a^{1/2}(1+1.3\frac{\theta}{A}), \text{ for } \theta_i = \frac{N_i - Z_i}{A_i},$$

but has small effect in the region of A and Z investigated here, owing to the small values of θ_i. The parameter a was taken to be equal to $\frac{A}{10}$, with no variation made with nuclear symmetry. Emission of deuterons or alpha particles was neglected, since these events would be quite improbable according to an equation analogous to (9). Hence $P_n + P_p = 1$ was assumed in each step of an emission cascade, and by using Eq. (9) the values of P_n and P_p for the first step of an evaporation process were calculated. These were called P_{n1} and P_{p1} to indicate that they referred to the first particle emitted. The temperature parameter, τ, appropriate to this step was computed from

$$\tau_{n1} = \frac{10\,E}{A}, \qquad (10)$$

and the spectrum for first-neutron emission from

$$\left.\frac{d\sigma}{dE}\right)_{n1} = \frac{P_{n1}\sigma_r}{\tau_{n1}^2}\,\epsilon\, e^{-\epsilon/\tau_{n1}}. \qquad (11)$$

The factor $\left.\frac{P_p}{P_n}\right)_2$, referring to second-particle emission, was then computed for each of the two possible residual nuclei, on the assumption of an average excitation energy $E_2 = E_1 - (Q_i + V_i + 2\,\tau_i)$, and the spectrum of "second neutrons" computed from

$$\left.\frac{d\sigma}{dE}\right)_{n2} = \frac{P_{nn}\sigma_r}{\tau_{nn}^2}\,\epsilon e^{-\epsilon/\tau_{nn}} + \frac{P_{pn}\sigma_r}{\tau_{pn}^2}\,\epsilon e^{-\epsilon/\tau_{pn}}, \qquad (12)$$

where $P_{nn} = (P_{n1})(P_{n2})$ and $P_{pn} = (P_{p1})(P'_{n2})$ (owing to different Q values involved in these reactions, we have $P_{n2} \neq P_{n2}'$). The computations were continued until the number of neutrons contributed above 5 Mev was negligible. A neutron spectrum predicted for Co^{59} is shown as a dashed curve in Fig. 37. The curve implied by the data and the predicted curve are somewhat similar, but the computed yield is nearly ten times that estimated from the experimental data.

For Ni^{58} and Ni^{60}, computed curves are very similar to that for Co^{59}, hence the correspondence with experimental observations is much poorer. The discrepancy in yields seems to be due to underestimation of the ratio F_p/F_n. Attention has already been called to this by Cohen,[31] who has furnished cross-section measurements made with 21.5-Mev protons on Ni^{58} which show quite clearly this departure. Cohen was able to measure the (p, 2p) and (p, pn) + (p, 2n) cross sections separately, finding 680 mb and 240 mb respectively. It is to be noted that the sum of these cross sections, 920 mb, is what would be computed for the reaction cross section σ_r. Using Eq. (9) one can calculate

$$\left.\frac{P_p}{P_n}\right)_1 = 0.12,$$

hence proton emission is very much more favorable than is predicted by evaporation theory. An estimate of the experimental ratio $\left.\frac{P_p}{P_n}\right)_1$ may be made from Cohen's data in the following way: the cross section σ_{pp}, for (p, 2p), may be set equal to $\sigma_r\ P_{p1}P_{p2}$, where P_{p1} is the emission probability of the first proton and P_{p2} is the emission probability of the second proton. Likewise

$$\left\{\sigma_{pn} = \sigma_r \quad P_{p1}\ P_{n2} + P_{n1}P_{p2}\right\},$$

and for definiteness we assume $P_{p1} = P_{p2}$ and $P_{n1} = P_{n2}$ (the effects of this assumption will be to underestimate the ratio $\left.\frac{P_p}{P_n}\right)_1$). Hence we have $\sigma_{pn} = 2\sigma_r P_p P_n$ and $\sigma_{pp} = \sigma_r P_p^2$, and the ratio $\left.\frac{P_p}{P_n}\right)_1 = \frac{2\sigma_{pp}}{\sigma_{pn}} = 5.66$. Thus the ratio of proton-to-neutron first emission is grossly underestimated by the statistical theory. It should be noted, however, that Ni^{58} is observed to have the lowest neutron yield of the targets studied in this work, hence the estimate of $\frac{P_p}{P_n}$ in this case would be expected to show the widest divergence from observation. Unfortunately, the cross sections σ_{pp} and σ_{np} were not available for the other targets. The data of Millburn,[12] however, have shown that the neutron-emission probability is overestimated for odd-Z nuclei distributed throughout the periodic table.

Another effect tending to reduce the total neutron yield by evaporation is that of lowered nuclear excitation due to escaping particles arising from direct interaction processes. Results of Monte Carlo type nuclear cascade calculations made by Metropolis et al.[32] can be extrapolated downward to 32-Mev proton bombarding energy, with the result that the average residual nuclear excitation for A near 64 may be expected to be on the order of 30 Mev, about 10 Mev below the maximum excitation of a compound nucleus with no direct emission. The effect of this lowered excitation is to reduce the "temperature" of each evaporation spectrum and hence lower the total particle yield. The elevated temperature values found when the total yield spectra were estimated would be expected to be due to inclusion of significant numbers of directly emitted neutrons with average energies higher than the evaporation spectra and concentrated in the forward hemisphere.

C. Concluding Remarks

The data obtained in this experiment have indicated that cross sections for neutron emission above 5 Mev depend on the isotopic composition of the target under consideration, as evidenced by the reduced neutron yield for Ni^{58} compared to that of Ni^{60}. Angular distributions of neutrons having energies greater than 5 Mev were found to be asymmetric, with a greater number of particles emitted into the forward hemisphere than into the backward direction. For the nickel isotopes, the variation in total yield and the character of the angular distributions seem to indicate that within the energy range under consideration there is a significant contribution of reactions, occurring near the nuclear surface, which depend upon the neutron occupation number of incompletely filled shells in the nucleus.

The differences in angular distributions between Co^{59} and Ni^{60} in the higher-energy regions, in which the reactions are known to be of the type (p, n), provide evidence that an incompletely filled proton shell affects the character of high-energy neutron emission. The differences in yield with energy were smaller than expected on the basis of a statistical theory, but the total neutron emission above 5 Mev was found to be small compared with reaction cross sections for the nuclei involved.

VII. ACKNOWLEDGMENTS

I would like to express sincere appreciation to Professor Burton J. Moyer for advice and encouragement throughout the course of this experiment. It would have been impossible to accomplish this work without the assistance of the Bubble Chamber Group directed by Professor Luis W. Alvarez; in particular, Mr. Arnold Schwemin provided chamber modifications rendering it suitable for use during the experiment and carried the responsibility for much of the operation during the entire program. A number of other operators contributed many hours during extended running periods. Excellent accelerator operation was provided by Mr. James Sirois and members of the linac crew. Several members of the Moyer research group willingly helped keep the bubble chamber filled with liquid hydrogen during accelerator-off periods late at night.

Mr. Harold E. Adelson collaborated closely during all phases of this experiment and made a simultaneous investigation of the neutron spectra of several light elements. Dr. Charles N. Waddell furnished helpful advice and aid during much of the planning and execution of the bombardment program. Film reading was done by Dr. Graham P. Conroy, Dr. Farhang Zabee, Miss Betty Blaine, Mr. Robert Brians, and Mr. William Wadman. Mr. Arthur W. Barnes designed and maintained much of the equipment associated with the film reader. The data-processing program was written for the IBM 650 by Mr. Kent Curtis.

This work was done under the auspices of the U.S. Atomic Energy Commission.

APPENDIX A

A. Track Reconstruction from Stereo Photographs

Consideration is first given to the problem of determining the location in real space of a point in a chamber viewed by a stereo camera without regard to the effects of refraction due to the glass face on the chamber and the liquid hydrogen inside. These effects are treated later. The geometry of the chamber-camera is illustrated schematically in Fig. 40. The plane of the diagram is denoted as the x-z plane, with the x direction taken to be the line of lens separation. The z axis is parallel to the lens axes; in this camera the lenses were parallel to each other. The origin of this coordinate system is on the inner surface of the front glass plate on the chamber. The coordinate z is thus a measurement of the depth of the point in the chamber.

Let (x'_p, y'_p, z'_p) be the Cartesian coordinates of a point p in the chamber,

x'_T and x'_B the coordinates of the top and bottom lens axis intersections with the plane $z = 0$ (front of chamber),

f be the lens-center-to-film distance,

x'_{p_T} and x'_{p_B} be the apparent top view and bottom view x coordinates of the point p,

and define

$$h_t = (x'_{p_T} - x'_p), \qquad g_T = (x'_T - x'_{p_T}),$$

$$h_b = (x'_p - x'_{p_B}), \qquad g_b = (x'_{p_B} - x'_B).$$

When the properties of similar triangles are utilized there arise two equations which can be solved for

x'_p and z'_p:

$$\frac{g_T}{f} = \frac{h_T}{z'_p} \quad \text{and} \quad \frac{g_b}{f} = \frac{h_b}{z'_p}$$

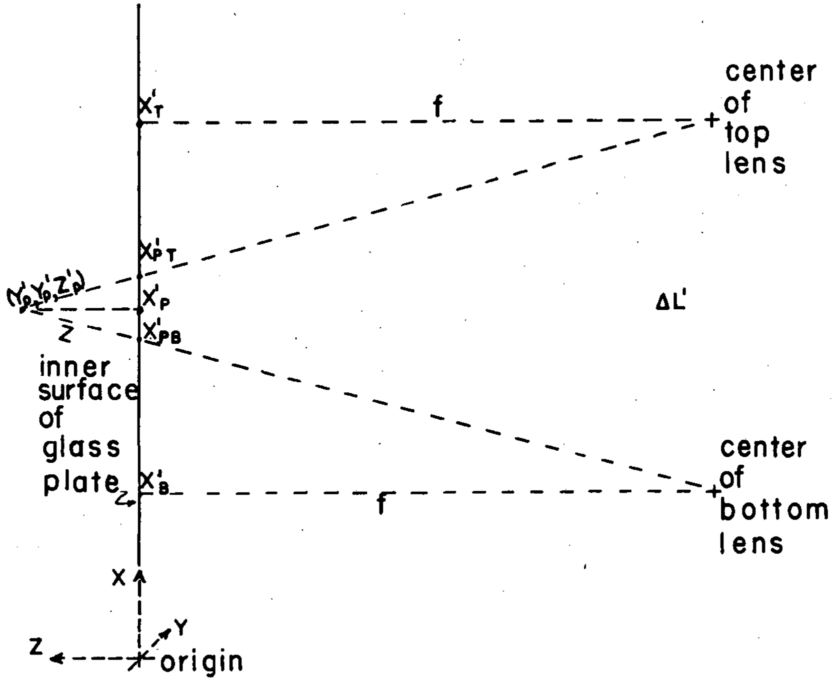

Fig. 40. Geometry of the stereo camera system in the plane defined by the lens axes and the stereo axis.

These have solutions

$$z'_p = f\,\frac{x'_{p_T} - x'_{p_B}}{g_T + g_b}\,, \qquad x'_p = \frac{g_b x'_T + g_T x_b}{g_T + g_b}\,.$$

When the quantities $(x'_T - x'_b) = \Delta L'$ (the lens separation) and $\Delta x'_p = (x'_{p_T} - x'_{p_B})$ are substituted, we have

$$z'_p = f\,\frac{\Delta x'_p}{\Delta L' - \Delta x'_p}\,, \tag{A-1}$$

$$x'_p = \frac{x'_{p_B}\,x'_T - x'_{p_T}\,x'_B}{\Delta L' - \Delta x'_p}\,. \tag{A-2}$$

Since the lens separation is in the x direction, both y coordinates y'_{p_T} and y'_{p_B} are equal. The determination of y'_p is carried out as indicated in Fig. 41. The equation

$$\frac{y'_p - y'_{p_T}}{z'_p} = \frac{y'_{p_T} - y'_T}{f}$$

yields

$$y'_p = \frac{z'_p}{f}\,(y'_{p_T} - y'_T) + y'_{p_T}\,. \tag{A-3}$$

An assumption is implicit: namely, that measurements were taken in real space. Hence it is necessary to modify Eq. (A-1) through (A-3) so that measurements taken in the "Oscar" coordinate system are transformed into real space coordinates. The optical boundries encountered are planar, so refractive effects are very nearly linear. Thus a linear correction may be applied which both treats refraction and transforms coordinate systems. A further advantage of this method is that differences in projection lenses are largely eliminated (it was not feasible to reproject through the camera lenses) and simultaneously the

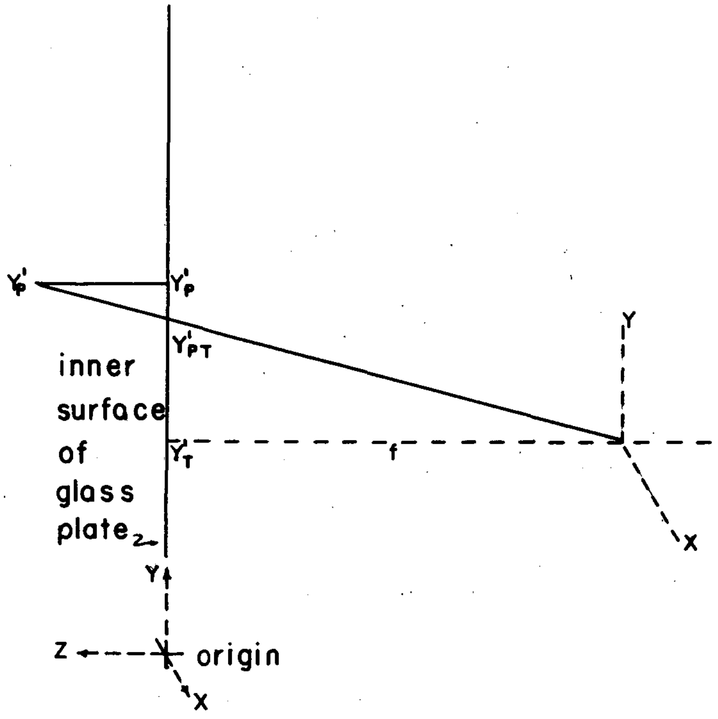

MU-16133

Fig. 41. Geometry of the correction to apparent y coordinates y'_{pt} and y'_{pb} to find the real coordinate y'_p.

magnification of the projection system is treated. The procedure is as follows: two fiducial marks which have a known separation Δx_f are chosen and their separation in the "Oscar" system, $\Delta x'_{f_T}$ in the top view and $\Delta x'_{f_B}$ in the bottom view is measured. Set

$g_{xT} = \dfrac{\Delta x_f}{\Delta x'_{f_T}}$ and $g_{xB} = \dfrac{\Delta x_f}{\Delta x'_{f_B}}$. Now coordinates of point p in the "Oscar" system are translated to the origin defined for the chamber system with the help of the fiducial-mark data contained on the master card for the view. Then the real-space coordinate x_p is determined by the equation

$$(2') \quad x_p = \frac{x_{p_B} x_T - x_{p_T} x_B}{\Delta L - \Delta x_p} ,$$

where

$$x_{p_B} = g_{x_B} x'_{p_B} ,$$

$$x_{p_T} = g_{x_T} x'_{p_T} ,$$

$$\Delta x_p = g_{x_T} x'_{p_T} - g_{x_B} x'_{p_B} ,$$

with

$\Delta L, x_T, x_B$ expressed in real-space coordinate system.

Two more factors, g_{y_T} and g_{y_B}, are determined in a similar manner. Then, after combining Eq. (A-1) with Eq. (A-3) to eliminate the factor $\frac{z'_p}{f}$ and transforming, one has the equation

$$y_p = \frac{\Delta x_p}{\Delta L - \Delta x_p} (y_{p_T} - y_T) + y_{p_T} . \qquad (A\text{-}3')$$

A factor to correct the z (depth) measurements is determined by calculating the apparent separation $\Delta z''$ of two fiducial marks located on the front and rear glass plates and separated by a distance Δz. The ratio $g_z = \frac{\Delta z}{\Delta z''}$ allows the equation for z_p to be written

$$z_p = g_z \left(\frac{\Delta x_p}{\Delta L - \Delta x_p} \right) . \tag{A-4}$$

The factors g_{x_T}, g_{x_B}, g_{y_T}, g_{y_B}, and g_z were determined for the optical system in use and then included as a part of the data-processing program.

The preceding analysis determines the true spatial location of a point from its apparent location in stereo photographs. The remaining problem is one of calculating the length of a track in the chamber and finding its orientation with respect to a fixed direction. In this work that direction is the y axis. The point in the chamber where the n-p collision took place is labeled point r and the point where the proton comes to rest point s. A cylindrical region is defined by the equation

$$(x_r - x_c)^2 + (z_r - z_c)^2 = R^2 , \tag{A-5}$$

where x_c and z_c are coordinates of the cylinder axis and R its radius. When the values x_r and z_r lead to a radius $R \geqslant R_0$ further calculation may be ceased. This constitutes the first chamber volume rejection. Next the length of the proton track may be computed from the straight-line equation

$$\ell = \left[(x_s - x_r)^2 + (y_s - y_r)^2 + (z_s - z_r)^2 \right]^{1/2} . \tag{A-6}$$

The y coordinates are required to satisfy the inequalities $y_r > y_1$ and $y_s < y_2$ to insure that the track starts and ends in the hydrogen. An answer card is produced in spite of such rejection, but the card carries a code punch indicating the reason for rejection. The polar angle θ is given by the equation

$$\cos \theta = \frac{(y_s - y_r)}{\ell} . \tag{A-7}$$

As indicated in Section III, rejection punch is included in the program for $\theta > 30^\circ$. Two equations are necessary to determine the azimuthal angle ϕ; they are

$$\cos\phi = \frac{f_s - f_r}{\ell \sin\theta}, \tag{A-8}$$

$$\tan\phi = \frac{x_s - x_r}{f_s - f_r}, \tag{A-9}$$

with the signs of Eqs. (A-8) and (A-9) locating the correct quadrant. The neutron energy can be calculated from the square of Eq. (A-7) and the proton energy E_p, which is determined from Eq. (A-6), by means of a range-energy table stored as a part of the processing program.

$$E_n = \frac{E_p}{\cos^2\theta} \tag{A-10}$$

B. Efficiency of the Bubble Chamber

Consider a flux f_0 of neutrons incident along the axis of a region of liquid hydrogen having a cylindrical shape, e.g., as in Fig. 42. The number of neutrons that survive passage through distance x, measured from the forward end of the cylinder, is given by the expression

$$n_s = f_0 \, e^{-\frac{N_0 \rho \sigma}{A} x},$$

where

n_s = number of survivors

ρ = density of hydrogen

σ = n-p scattering cross-section

N_0 = Avogadro's number

A = atomic weight of hydrogen

The total number of interactions in the distance x is then

$$N = f_0 F \left(1 - e^{-\frac{N_0 \rho \sigma}{A} x}\right),$$

where F is the fraction of the n-p scattering cross section that contributes to the observed encounters. Beyond a given distance χ,

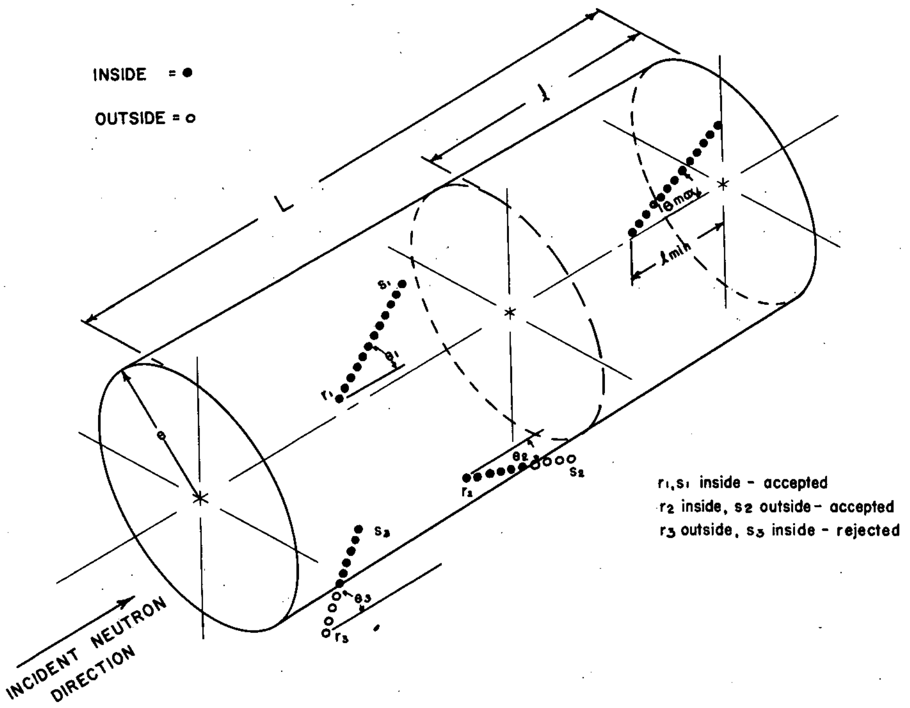

MU-16134

Fig. 42. Geometry of acceptable track region. The region with length l has a track-containment efficiency of less than 100%. Proton-recoil tracks begin at point r and stop at point s; track-acceptance criteria are illustrated.

it is possible for tracks corresponding to some energies to leave the end of the region; they are rejected by the analysis scheme. Thus not all interactions in the region are contained and recorded. The purpose of this section is to derive a detection-efficiency factor which accounts for both the probability of n-p collisions and the loss of some proton recoils from these collisions. This may be done readily in the following way. Consider the diagram in Fig. 42. For an energy E_n there is a length ℓ corresponding to a proton recoil of energy $E_p = E_n$, i.e., a proton moving off straight ahead. This length ℓ represents that distance from the rear of the chamber at which recoil protons from neutrons having energy E_n begin to get lost. Consider now an arbitrary point in the region between $x = (L - \ell)$ and $x = L$, where L is the length of the cylinder. Recoil protons that make an angle θ greater than some minimum value θ_{min} are contained, while those having θ less than θ_{min} are lost. Since the dependence of proton track length on proton energy can be expressed as $\ell = aE^u_p$, with a and u known, θ_{min} can be determined for a given position and energy. Since there is a maximum angle accepted by the analysis scheme, there is a minimum distance for acceptable tracks, $(L-\ell_{min})$, which is determined by the condition that a proton track at an angle θ_{max}, resulting from a neutron having energy E, will just reach a plane determined by the cylinder's end. It should be pointed out that the cylinder selected in the chamber had L small enough so that this latter condition held for all off-axis points; only the beginning of a track was required to lie inside the cylinder. As shown in Section III, the expected angular distribution of recoil tracks is $\frac{dn}{d\theta} = \sin 2\theta d\theta$, so that the fraction of n-p encounters occurring in the ~~region~~ located between x and $x+dx$ is

$$\frac{\displaystyle\int_{\theta_{min}}^{30^\circ} \sin 2\theta d\theta}{\displaystyle\int_{0}^{30^\circ} \sin 2\theta d\theta} = \frac{\frac{1}{2}\left(\cos 2\theta_{min} - \frac{1}{2}\right)}{\frac{1}{4}} = (2 \cos 2\theta_{min} - 1),$$

where θ_{max} has been set to 30° as in the analysis scheme. The quantity

$\theta_{\min}$ is found from the expressions

$$\ell = aE_p^{\;u} = aE^u_{\;n} \cos^{2u}\theta$$

and

$$x = \ell \cos\theta = aE^{2u}\cos^{2u+1}\theta$$

or

$$\cos\theta(x)_{\min} = \left(\frac{x}{aE^{2u}}\right)^{\frac{1}{2u+1}} .$$

The number of interactions observed between x and $x+dx$ is

$$-\frac{df}{dx}\,(2\cos 2\theta_{\min} - 1)\,dx,$$

so that the total number of interactions observed in the chamber is

$$N_{obs} = Ff_0\left(1-e^{\frac{-L-\ell}{\lambda}}\right) - \frac{Ff_0}{\lambda}\int_{\ell}^{r_{\min}} e^{-\frac{x}{\lambda}}$$

$$(2\cos 2\theta_{\min}-1)dx,$$

where λ has been set equal to $\frac{A}{N_0\rho\sigma}$.

The flux f_0 is to be determined, therefore we have

$$f_0 = F^{-1} N_{obs}\left[\left(1-e^{\frac{-L-\ell}{\lambda}}\right) - \frac{1}{\lambda}\int_{\ell}^{r_{\min}} e^{-\frac{x}{\lambda}}\,(2\cos 2\theta_{\min}-1)dx\right]^{-1} .$$

With the expression for $\cos 2\theta_{\min}$ substituted, the integral above may be evaluated to the required degree of precision by expanding the exponential function into a power series and setting the constant u equal to 1.84. The result is

$$f_0 = F^{-1} N_{obs}\left[\left(1-e^{-\frac{L-\ell}{\lambda}}\right) - \frac{e^{-L/\lambda}}{\lambda}\left\{3\lambda(e^{\ell/\lambda} - e^{.510\ell/\lambda}) - \right.\right.$$

$$\left.\left. -4\left(.433\ell + \frac{.331\ell^2}{\lambda} + \frac{.131\ell^2}{\lambda^2} + \frac{.0356\ell^4}{\lambda^3}\right)\right\}\right]^{-1}$$

The included scattering fraction F in this expression also shows an energy dependence. For neutron energies of less than 10 Mev the angular distribution of n-p scattering can be regarded as isotropic in the center-of-momentum system of the free neutron and proton. In this case the fraction F of all scattering events observed in the data-analysis system is

$$F = \frac{\frac{\sigma_T(E)}{4\pi}\int_0^{60^\circ}\sin\theta\, d\theta\int_0^{2\pi} d\phi}{\sigma_T(E)} = \frac{1}{4} \quad \text{for } E \lesssim 10 \text{ Mev.}$$

Above 10 Mev a small correction for anisotropy of n-p scattering is needed. In this region the scattering appears to be composed of contributions of S and D partial waves, so that the cross section may be written

$$\sigma(\theta_c) = \sigma_{90^\circ}\,(1 + A\cos^2\theta_c)\ .$$

In this work, the formulation of Gammel^{33} has been adopted in order to compute the fraction F. The anisotropy is taken to vary as E^2 and required to approach the measured value at 90 Mev. Hence the cross section may be written

$$\sigma(\theta_c, E) = \frac{\sigma_T(E)}{4\pi}\left[\frac{1 + 2\left(\frac{E}{90}\right)^2\cos^2\theta_c}{1 + \frac{2}{3}\left(\frac{E}{90}\right)^2}\right]$$

Then F may be computed from the integral

$$F = \frac{2\pi}{\sigma_T(E)}\int_0^{60^\circ}\sigma(\theta_c, E)\sin\theta_c\, d\theta_c = \frac{6 + 7\left(\frac{E}{90}\right)^2}{24 + 16\left(\frac{E}{90}\right)^2} \quad \text{for } E > 10 \text{ Mev.}$$

The quantity $\frac{f_0(E_n)}{N_{obs}}$ is the factor by which raw neutron data must be multiplied to determine the incoming neutron intensity. A table of numerical values was constructed for use in the data-reduction program.

The efficiency of the bubble chamber as a neutron detector is defined to be the reciprocal quantity, $\frac{N_{obs}}{f_0(E_n)}$. A graph of the efficiency as a function of neutron energy is shown in Fig. 43.

C. Line Shape of Neutrons from t(d, n)He^4 Reaction

The tritium-titanium target employed for production of 14-Mev neutrons in this work had a structure such that the incoming deuteron beam could undergo some Coulomb scattering. Owing to the limit of thickness of the target it was necessary to reduce the 4-Mev deuteron energies 2 Mev by requiring their passage through a degrading foil; a 36.7-mg/cm^2 gold foil was employed. It was thus desirable to examine the kinematical effects of Coulomb scattering arising both from the gold foil and the tritium-titanium target in which the deuterons were brought to rest.

It was assumed that because of multiple Coulomb scattering the beam of deuterons might be considered as distributed about the average beam direction by an expression of the form

$$p(\theta)d\theta = \frac{1}{\sqrt{2\pi}} e^{-\frac{\theta^2}{\overline{\theta^2}}} , \qquad \text{(C-1)}$$

where $P(\theta)$ is the probability of finding a deuteron with deviation θ between θ and $\theta + d\theta$, and $\overline{\theta^2}$ is the mean-square scattering angle. Values for $\overline{\theta^2}$ were computed from an expression developed from that given in Fermi's lecture notes on nuclear physics.[34]

$$\overline{\theta^2} = \frac{2\pi z^2 \epsilon_e^2 r_e^2}{A} \sum_{i=1}^{n} \frac{X_i}{E_i^2} \ln\left(\frac{a_0}{r_e} \frac{E_i}{z^{4/3}\epsilon_e}\right), \qquad \text{(C-2)}$$

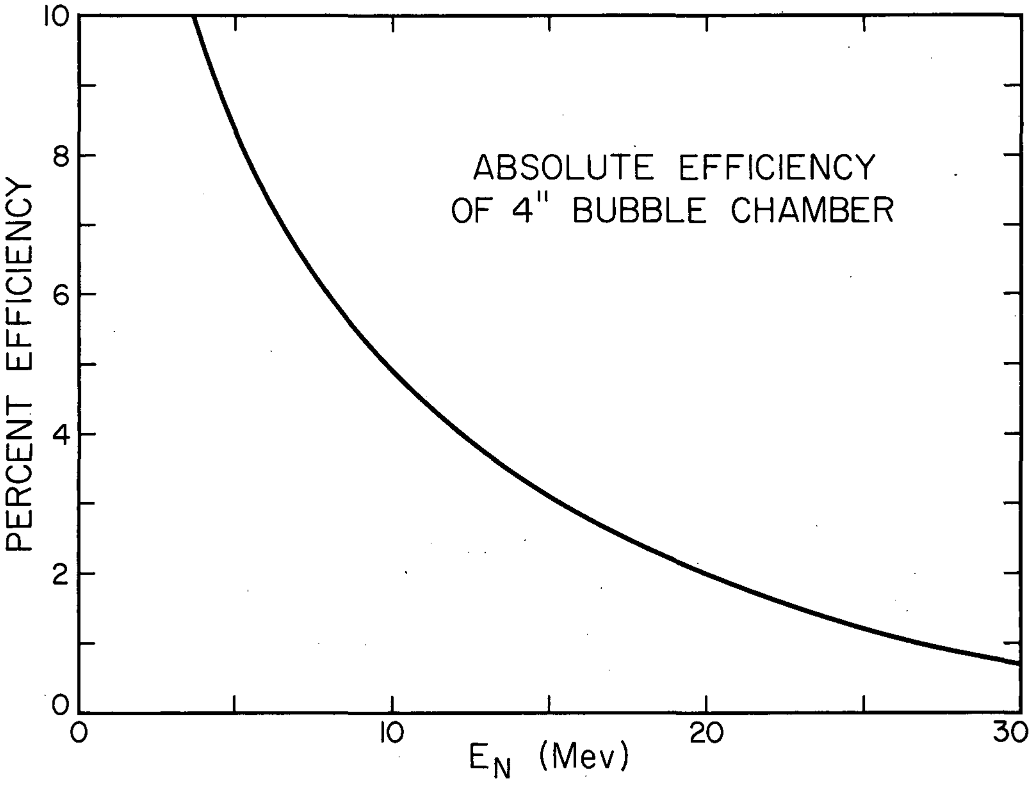

MU-14944

Fig. 43. Efficiency of the four-inch hydrogen bubble chamber for detection of neutrons.

where

ϵ_e is the electron rest energy,

r_e is the classical electron radius,

χ_i is the areal density of the ith matter layer,

E_i is the particle kinetic energy in the ith layer.

For purposes of calculating neutron-energy shifts, the projection of angle θ onto the plane containing the target, detector, and beam line was desired. It can be shown[35] that the mean square projected angle of scattering, $\overline{\theta_p^2}$, is related to $\overline{\theta^2}$ by the expression

$$\overline{\theta_p{}^2} = \frac{1}{2}\,\overline{\theta^2} \quad . \tag{C-3}$$

By use of Eqs. (C-2) and (C-3), the $\overline{\theta_p{}^2}$ for the gold foil was calculated by considering eight layers; the range-increment data were computed by adjusting the lead data calculated by Aron et al.[19] Thus $\overline{\theta_p{}^2}$ was found to be 3.06×10^{-2} for passage of deuterons going from 4 to 2 Mev. An energy-loss curve for tritium-titanium was developed by using the method adopted by Benveniste and Zenger[36] from proton energy-loss data in H_2, Al, and Cu given by Allison and Warshaw.[37] This curve is reproduced in Fig. 44. From the energy-loss curve, Fig. 44, and Eqs. (C-2) and (C-3), the root-mean-square projected scattering angle for deuterons in tritium-titanium was calculated. The variation of this angle with deuteron kinetic energy is shown in Fig. 45.

A curve giving the relative yield of neutrons vs. deuteron energy was computed from the tritium-titanium energy-loss curve and the curve for neutron-production cross section vs. deuteron-energy given by Fowler and Brolley.[23] This yield curve is reproduced in Fig. 46. Tables of deuteron-neutron kinematics for the $t(d,n)He^4$ reaction included in Reference 23 were utilized to find neutron energy corresponding to particular deuteron scattering angles. A tabulation of areas under the curve for Eq. (C-1) (with $\overline{\theta^2}$ replaced by $\overline{\theta_p^2}$) published in mathematical tables with the variable $t = \frac{\theta}{\sqrt{\overline{\theta_p^2}}}$ allowed calculation of relative neutron yields by taking differences between lower and upper tabular entries.

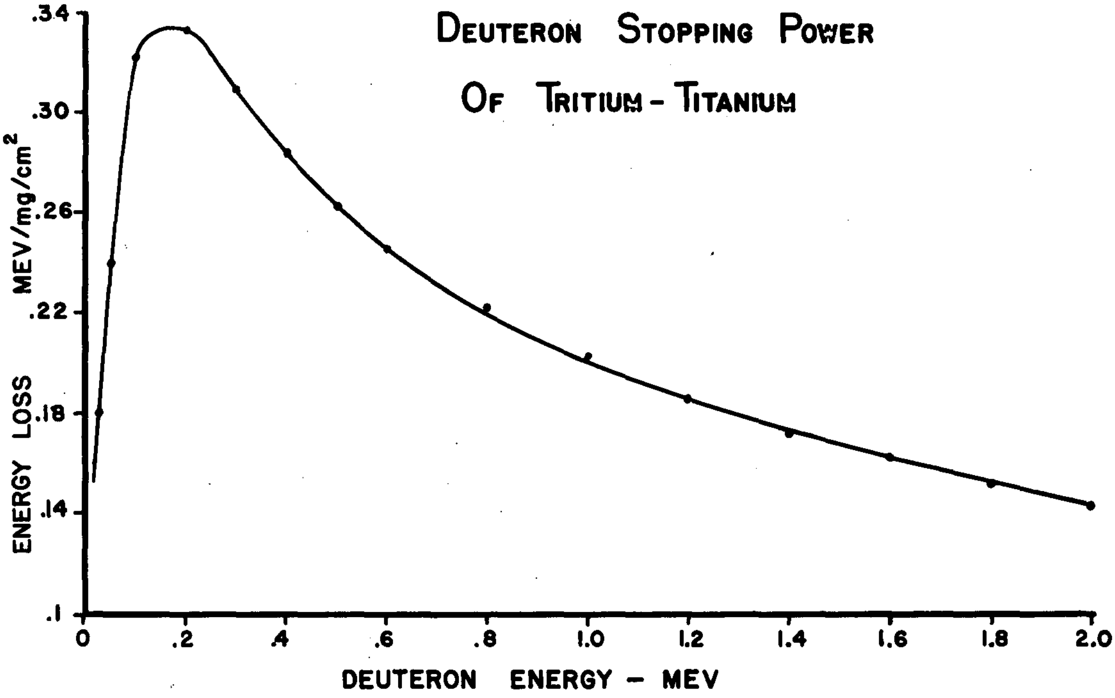

MU-16136

Fig. 44. Stopping power of tritium-titanium for deuterons.

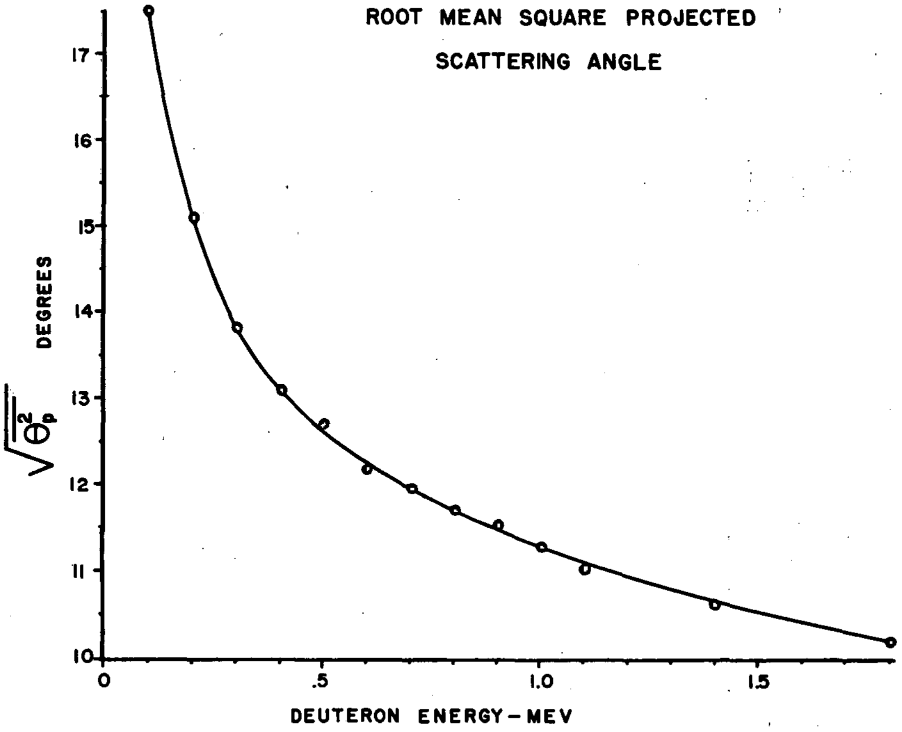

MU-16135

Fig. 45. Root-mean-square projected scattering angle in degrees for deuterons in tritium-titanium.

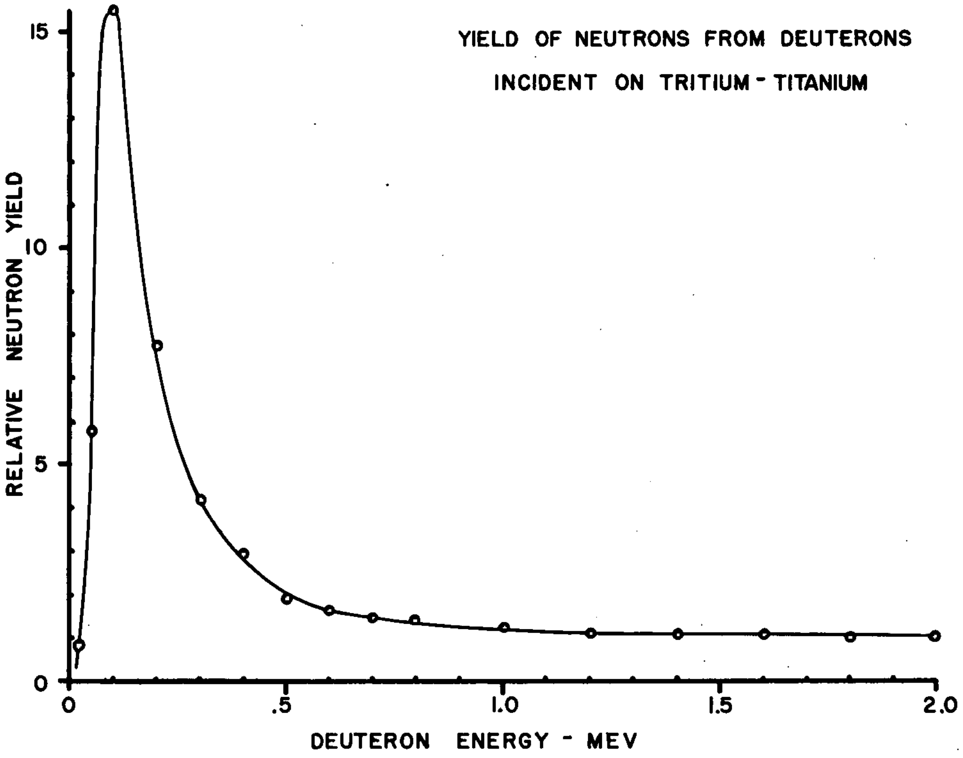

MU-16137

Fig. 46. Calculated yield of neutrons as a function of deuteron energy within a tritium-titanium target.

Thirteen layers of tritium-titanium were treated separately and the relative yields of neutrons in 0.2-Mev increments were summed to get the spectrum shape shown in Fig. 13.

REFERENCES

1. V. Weisskopf, Revs. Modern Phys. 29, 174 (1957).
2. N. Bohr, Nature 137, 344 (1936).
3. Weisskopf and Ewing, Phys. Rev. 57, 472 (1940).
4. L. Wolfenstein, Phys. Rev. 82, 690 (1951).
5. Hauser and Feshbach, Phys. Rev. 87, 336 (1952).
6. Blatt and Weisskopf, Theoretical Nuclear Physics (Wiley, New York, 1952).
7. R. Serber, Phys. Rev. 72, 1114 (1947).
8. Skyrme and Williams, Phil. Mag. 42, 1187 (1951).
9. Eisberg and Igo, Phys. Rev. 93, 1039 (1954).
10. S. Butler, Phys. Rev. 106, 272 (1957).
11. Tai, Millburn, Kaplan, and Moyer, Phys. Rev. 109, 2086 (1958).
12. George Millburn, Neutron Yields from Thick Targets Bombarded by 18- and 32-Mev Protons (thesis), UCRL-3320, Feb. 1956.
13. Austern, Butler, and McManus, Phys. Rev. 92, 350 (1953).
14. Mayer and Jensen, Elementary Theory of Nuclear Shell Structure (Wiley, New York, 1955).
15. Edward Gross, The Absolute Yield of Low-Energy Neutrons from 190-Mev Proton Bombardment of Gold, Silver, Nickel, Aluminum, and Carbon (thesis), UCRL-3330, Feb. 1956.
16. P. Gugelot, Phys. Rev. 93, 425 (1954).
17. D. Allan, Proc. Phys. Soc. (London) A70, 195 (1957).
18. Parmentier and Schwemin, Rev. Sci. Instr. 26, 954 (1955).
19. Aron, Hoffman, and Williams, Range Energy Curves, AECU-663, 1949.
20. Alvarez et al., Rev. Sci. Instr. 26, 111 (1955).
21. Harry C. Dittler and Thomas F. Gerecke, Liquid Hydrogen Bubble Chambers (MS thesis), UCRL-2985, May 1955.
22. Fowler and Brolley, Revs. Modern Phys. 28, 103 (1956).
23. M. Lynn Stevenson, Estimated Density of Superheated Normal Liquid Hydrogen, UCRL Engineering Note M13A, December 12, 1956.
24. Hughes and Harvey, Neutron Cross Sections, BNL-325, July 1955.

25. Quisenberry, Scolman, and Nier, Phys. Rev. 104, 461 (1956).

26. J. Riddell, A Table of Levy's Empirical Atomic Masses, CPR-654, Chalk River, Ontario, July 1956.

27. A. Wapstra, Physica 21, 385 (1955).

28. Cohen, Newman, and Handley, Phys. Rev. 99, 723 (1955).

29. Harris B. Levy, A New Empirical Mass Equation: I. Atomic Masses in the Fission Production Region, UCRL-4588, Nov. 1955.

30. K. LeCouteur, Proc. Phys. Soc. (London) A63, 259 (1950).

31. Cohen and Newman, Phys. Rev. 99, 718 (1955).

32. Metropolis, Bivins, Storm, Turkevich, Miller, and Friedlander, Phys. Rev. 110, 185 (1958).

33. Bame, Haddad, Perry, and Smith, Rev. Sci. Instr. 28, 997 (1957).

34. Orear, Rosenfeld, and Schluter, Nuclear Physics, Revised Ed. (University of Chicago Press, Chicago, 1953).

35. B. Rossi, High Energy Particles (Prentice Hall, New York, 1952).

36. J. Benveniste and J. Zenger, Information on the Neutrons Produced in the $H^3(d,n)He^4$ Reaction, UCRL-4266, Jan. 1954.

37. Allison and Warshaw, Res. Modern Phys. 25, 779 (1953).